

Review

Biological Bone and Replacement Materials in Grinding: Force Model and Processing Capability

Xianggang Kong, Chuankun Li, Zhonghao Li, Min Yang *, Xin Cui, Mingzheng Liu, Benkai Li, Yanbin Zhang, Xiao Ma and Changhe Li

Key Lab of Industrial Fluid Energy Conservation and Pollution Control, Ministry of Education, Qingdao University of Technology, Qingdao 266520, China; 15006563212@163.com (X.K.); 17685471508@163.com (C.L.); ytlizh@163.com (Z.L.); cxinxin5240@163.com (X.C.); lmzzz654321@163.com (M.L.); lbk17082@163.com (B.L.); zhangyanbin1 qdlg@163.com (Y.Z.); gdmaxiao@126.com (X.M.); sy lichanghe@163.com (C.L.)

* Corresponding author. E-mail: 18266487809@163.com (M.Y.)

Received: 17 December 2024; Revised: 25 December 2024; Accepted: 8 January 2025; Available online: 16 January 2025

ABSTRACT: Grinding is widely used in orthopedic surgery to remove bone tissue material, but due to the complex and brittle structure of bone, it is prone to mechanical stresses that cause cracks and damage to the bone tissue. Furthermore, bone replacement materials typically have high hardness, strength, and brittleness, which lead to increased tool wear and damage, such as cracks and deformation during grinding. Therefore, ensuring the surface quality of bone and replacement materials during the grinding process has become a critical issue. This necessitates the development of grinding force models that consider various processing parameters, such as feed rate and cutting depth, to guide industrial production. However, currently, research on the grinding force prediction models for bone tissue and its replacement materials is relatively scarce, and there is a lack of corresponding grinding force model reviews for unified guidance. Based on this, this article focuses on bone grinding technology and, conducts a critical comparative analysis of the grinding force models for bone tissue and its replacement materials, and then summarizes the grinding force prediction models in the grinding process of bone tissue and bone replacement materials. First, according to the material types and material removal mechanisms, the materials are categorized into bone tissue, bio-inert ceramics, and bio-alloys, and the material removal process during grinding is analyzed. Subsequently, the grinding force prediction models for each material and the accuracy errors of each model are summarized. The paper also reviews the application of these grinding force prediction models, explaining how processing parameters such as feed rate and cutting depth influence grinding forces and their interrelationship. Finally, in light of the current issues in the grinding of bone tissue and replacement materials, potential future research directions are proposed, aiming to provide theoretical guidance and technical support for improving the grinding quality of bone tissue and its replacement materials.

Keywords: Grinding; Bone; Bio-inert ceramics; Bio-alloys; Grinding force



© 2025 The authors. This is an open access article under the Creative Commons Attribution 4.0 International License (https://creativecommons.org/licenses/by/4.0/).

1. Introduction

Bone grinding technology plays a crucial role in clinical medicine, particularly in the fields of bone tissue repair, joint replacement, and fracture healing [1]. With the aging population and the increasing prevalence of orthopedic diseases, the demand for high-precision and high-efficiency processing of bone tissue and replacement materials in orthopedic surgery is also rising [2]. As a high-precision machining technique, bone grinding has made significant progress in shaping bone and implant materials [3], surface treatment [4], and optimizing contact performance [5], and has gradually become one of the important methods in the manufacturing of modern orthopedic medical devices and repair materials. At the same time, with the rapid development of biomedical engineering and materials science [6], especially improvements in biocompatibility, durability, and mechanical properties, the types and applications of bone tissue and replacement materials have expanded [7]. Notably, bioalloys, ceramics, and other replacement materials are widely used in artificial joints, spinal implants, and craniofacial repairs [8]. The processing of these materials requires not only precise techniques [9] but also strict biological compatibility and mechanical adaptability to ensure the long-term stability of the implants and the effective recovery of patients [10].

Bioalloys can integrate well with human tissues (such as bones and soft tissues), avoiding immune rejection and meeting the clinical requirements for mechanical properties and biodegradability [11]. Common bioalloys include titanium alloys, cobalt-based alloys, and magnesium alloys. With titanium alloys and magnesium alloys showing significant advantages in clinical bone replacement [12]. Titanium alloys are lightweight, have high specific strength, and can provide mechanical strength similar to that of bone [13]; they also have excellent corrosion resistance, meaning they do not corrode even during long-term use in the body [14]. Titanium has good biocompatibility and is unlikely to cause allergic reactions, which is why it is widely used in artificial joints, fracture fixation devices, and dental implants [15]. Magnesium alloys, on the other hand, have a density and mechanical properties closer to that of bone, along with unique biodegradability [16]. This means that magnesium alloys are gradually absorbed by bone tissue during use in the body, unlike traditional metallic materials that persist for long periods, greatly reducing the likelihood of complications and the need for secondary surgeries. Additionally, magnesium ions promote bone growth and repair, enhancing bone density and strength [17], which demonstrates the tremendous potential of magnesium alloys in bone defect repair and tissue engineering [18].

Bioceramics are a class of ceramic materials that are biocompatible and can be used long-term in a biological environment without causing immune rejection [19]. They are widely used in medical fields such as bone repair, joint replacement, and dental implants [20]. Bioceramics are classified into three main types: bioinert ceramics, bioactive ceramics, and biodegradable ceramics [21]. Among them, bioactive ceramics promote bone healing and bond with bone tissue, but they have relatively low mechanical strength, are prone to brittle fracture, and cannot withstand high loads, making them unsuitable for areas requiring long-term weight-bearing [22]. Biodegradable ceramics can gradually degrade and promote bone repair, but their degradation rate is difficult to control [21]. If the degradation occurs too quickly, it may lead to insufficient support from the implant, affecting the bone healing process and even causing fractures or instability [22]. Compared to these two types of ceramics, bioinert ceramics combine the advantages of both while overcoming their drawbacks [23]. Bioinert ceramics exhibit a lower risk of immune reactions during interaction with biological tissues, effectively reducing rejection phenomena [24]. Moreover, these ceramic materials can resist the corrosion of body fluids, extend the service life of implants, and possess excellent load-bearing capacity, making them suitable for applications involving heavy loads [25]. Therefore, bioinert ceramics (such as alumina Al₂O₃ andzirconia ZrO₂) are commonly used materials in clinical bone replacement due to their unique properties [26].

In the processing of bone tissue repair, joint replacement, and implant materials before they are applied to the human body, grinding is an essential and crucial step [27]. Through grinding, the shape, size, and surface smoothness of implants can be precisely adjusted to ensure a perfect fit between the implant and bone tissue or joint surfaces, enhancing their biocompatibility and functionality. However, the grinding process may cause some defects in the material: during the grinding of bone tissue, excessive grinding force may result in irreversible damage [28], such as excessive harm to the bone tissue and surrounding nerve tissues, which affects healing [29], Although bioalloys (such as titanium alloys) have good mechanical properties [30], microcracks or surface roughness may be generated during grinding, affecting their long-term stability [30]. Bioinert ceramics like alumina and zirconia, while having high hardness and wear resistance, are prone to brittle fracture or surface microcracks during grinding [31], which reduces their mechanical properties and may even affect their long-term use in the body [32–36]. Therefore, reducing grinding force during the process, improving the processing quality of bone tissue and replacement materials, and ensuring machining accuracy are important factors in the development of bone grinding technology [17,37–42].

Many scholars have studied the grinding forces generated during the grinding process of bone repair and bone replacement materials [42]. Research has found that the variation in grinding force is influenced by a combination of processing parameters such as spindle speed, feed rate, cutting depth, and ultrasonic vibration frequency [43]. As shown in Figure 1, a visual analysis of the relevant literature on grinding bone and replacement materials was conducted using data analysis of VOSviewer. The keyword clusters in the figure are mainly composed of "bone", "ceramics", "grinding", etc. The size of the bubbles represents the frequency of the appearance of the keywords, and the crisscross lines in the middle reflect the corresponding correlations among the keywords. Among them, the green cluster mainly includes "bone", "biocompatibility", etc., which is mainly about the research on relevant properties. The red cluster is for the research on grinding, grinding processing and related defects. The yellow and blue clusters, respectively, correspond to the research on the mechanical properties of bioceramics and bioalloys. It can be clearly found that in the research on the grinding force of bone replacement materials, the research on the grinding force and prediction models is relatively scarce, and the respective characteristics of materials will also have a non-negligible impact on the grinding quality during the grinding processing. Meanwhile, when establishing the grinding force prediction model, emphasis should be placed not only on the processing parameters but also on crucial factors such as physical behaviors, surface integrity,

inherent mechanical properties of the materials, and other relevant factors. Therefore, establishing a grinding force model for the grinding process is both a necessary and challenging task. However, literature searches reveal that research on grinding forces for bone tissue and replacement materials has primarily focused on the effects of different processing parameters on grinding force and surface quality, with relatively little research on the theoretical aspects of grinding force prediction models. Furthermore, there is a lack of comprehensive reviews on the grinding force models for bone tissue and replacement materials.

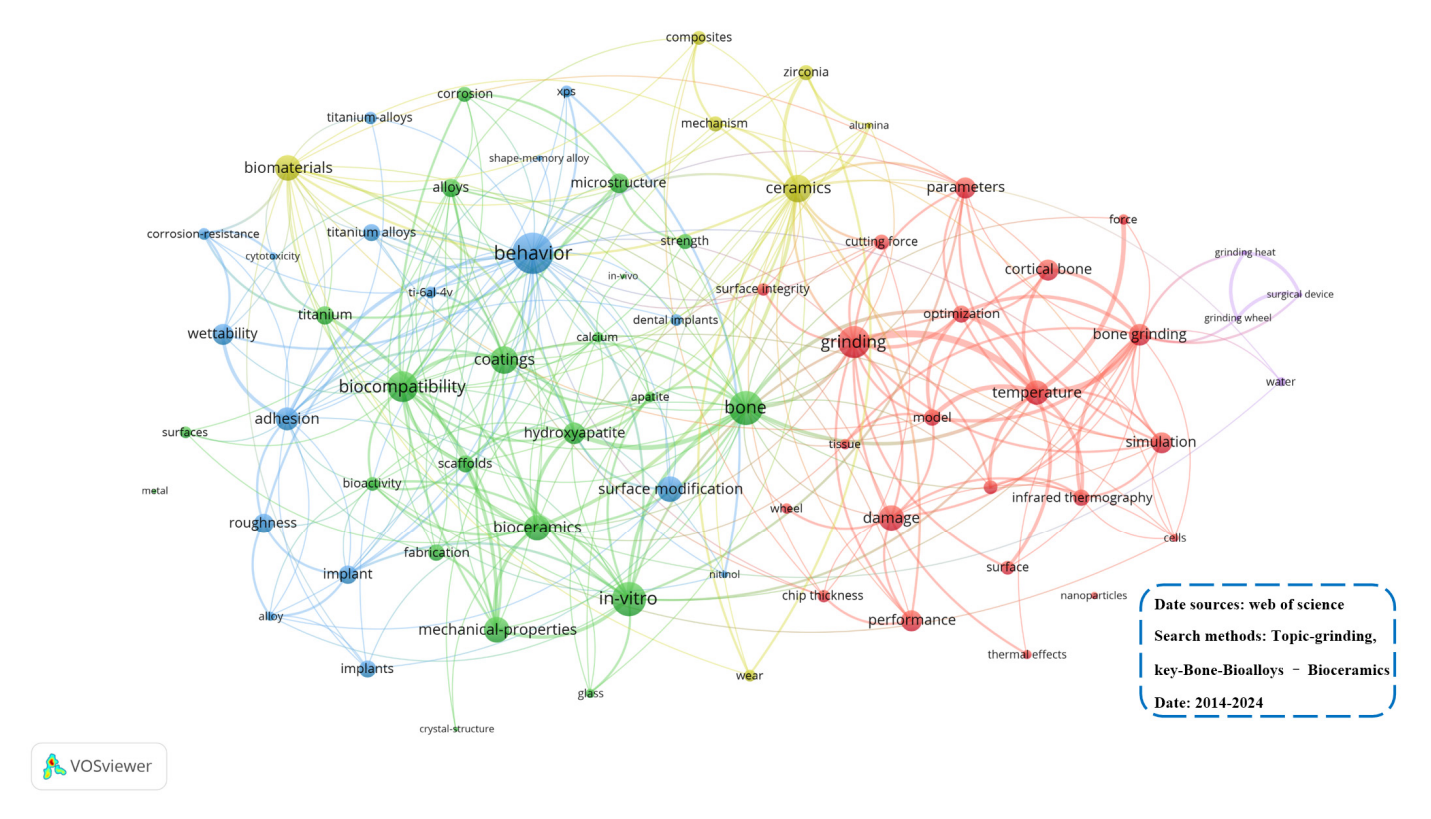


Figure 1. Keywores co-occurrence network map.

The research approach of this paper is shown in Figure 2. The paper analyzes bone tissue and two types of replacement materials: bioinert ceramics and bioalloys. It examines the material removal mechanisms for each of the three materials and, based on the differences in material removal principles, analyzes and summarizes the grinding force prediction models under various variable conditions for bone, bioalloy, and bioinert ceramic materials. The applications of each model are also summarized, and the effects of different processing parameters on the grinding force are explored.

To address the aforementioned issues, this paper proposes future research directions for the grinding technology of bone tissue and bone replacement materials. It summarizes the grinding force prediction models for bone tissue and replacement materials during the grinding process. The paper presents grinding force prediction models for bone, bioinert ceramics, and bioalloys, which are established based on different material removal mechanisms. These models are developed from various perspectives and approaches. Additionally, the paper summarizes the application of grinding force prediction models and related experimental validations. It explores the influence and mapping relationships between different processing parameters, such as feed rate and, cutting depth, and grinding force. The aim is to provide theoretical guidance and support to improve the processing quality during the grinding of bone tissue and its replacement materials.

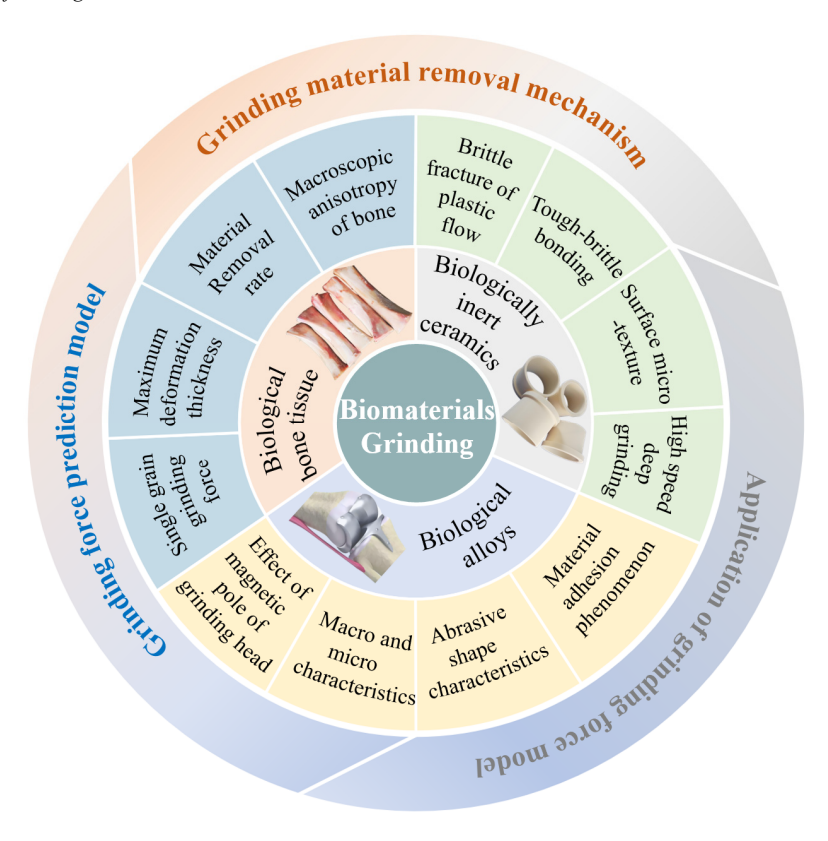


Figure 2. Review narrative logic.

2. Biological Bone Tissue

2.1. Material Removal Mechanism

Biological bone tissue is a hard and brittle biological tissue with complex structures and anisotropic properties [44–48]. These characteristics enable bone tissue to withstand various forms of stress and loads. From the perspective of mechanical properties, the arrangement of osteons and the directional layout of interstitial laminae in the microstructure are decisive factors. Together, they contribute to the significant anisotropic characteristics of biological bone in terms of elastic modulus, shear strength, and fracture toughness [49–53]. Mechanical processing methods for biological bone tissue include grinding, milling, drilling, and energy field-assisted processing, among which grinding is a relatively commonly used method for processing biological bone tissue.

In the grinding process of bone tissue, micro-grinding is one of the most common methods (as shown in Figure 3). Micro-grinding involves the removal of a small amount of bone tissue multiple times using fine abrasive particles on a micro-grinding tool to ensure precision and safety in operation. During the grinding process, grinding forces and grinding heat are inevitably generated. These forces and heat, when acting on human tissue, can inevitably affect the surrounding tissues and, in severe cases, lead to irreversible damage to neural tissue. Wang et al. [54] reviewed the material removal mechanisms and mechanical behaviors of biological bone materials under different processing techniques, outlining the current development status of bone materials and the challenges they face. There is a risk of material cracking or damage during the grinding of biological bone tissue, posing a significant challenge in orthopedic surgery. In particular, when the undeformed chip thickness ($h_{\rm m}$) falls between the minimum chip thickness and the critical thickness for plastic deformation, the heat generated during the grinding process is relatively low, effectively avoiding thermal damage to the biological bone tissue.

Regarding the grinding mechanism of biological bone materials, Yang et al. [55] proposed a new process method involving ultrasonic vibration-assisted nanoparticle spray cooling. This method effectively reduces grinding forces and grinding heat compared to other processes. Yang et al. [56] established models for the maximum undeformed chip thickness (h_{max}) and heat flux density. Experiments showed that, compared to spray cooling, as the volume fraction of nanoparticles increased, the surface temperature of the bone showed a downward trend. Additionally, considering the size effect of the transition from ductile to brittle behavior, mathematical models were developed for the minimum chip thickness and critical undeformed chip thickness in micro-grinding of biological bone. Therefore, biological bone material is a quasi-brittle, high-density viscoelastic composite. During material removal, it generally undergoes both

plastic removal and brittle fracture. Grinding forces and grinding temperatures have a significant impact on the grinding process of bone, so the material removal process must be discussed and analyzed when constructing a grinding force model.

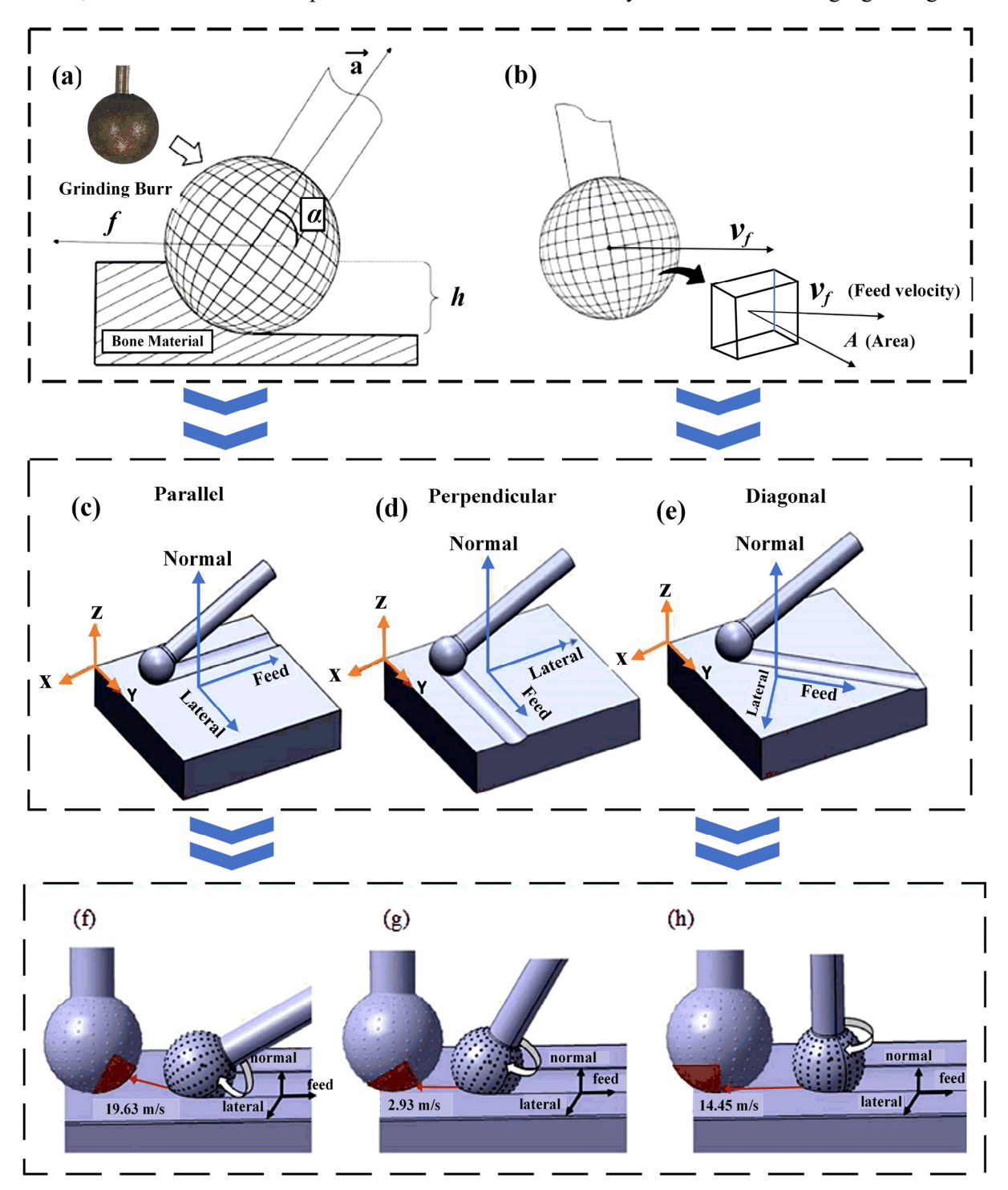


Figure 3. Grinding models in Danda's study: (a) Schematic diagram of grinding, (b) area swept by elements of the grinding tool, (c) parallel grinding, (d) perpendicular grinding, (e) diagonal grinding, (f) relative motions at 30°, (g) relative motions at 60°, (h) relative motions at 90°.

2.2. Grinding Force Mode

Zou et al. [57] determined the total grinding force by calculating the aggregate number of grains engaged in the grinding process and subsequently developed a bone grinding force model. This model offers enhanced precision in calculating the magnitude of the three-directional grinding force. Their research revealed that the anisotropy of bone tissue significantly influences the grinding force, particularly in relation to the spindle inclination angle and feed direction. Notably, variations in the spindle inclination angle result in changes in the linear velocity of the grains, which in turn affect the grinding force. However, this model has not yet taken into account the influences of abrasive particle

size, movement trajectory, and material properties of bone tissue on the model, as well as the applicability of the model. By formulating hypotheses regarding the grain count, the component forces along the x, y, and z axes can be derived as:

$$\begin{cases} F_{x} = r_{x} \cdot \sum_{i=1}^{N} (F_{et}(i) + F_{en}(i)) \\ F_{y} = r_{y} \cdot \sum_{i=1}^{N} (F_{et}(i) + F_{en}(i)) \\ F_{z} = r_{z} \cdot \sum_{i=1}^{N} (F_{et}(i) + F_{en}(i)) \end{cases}$$
(1)

where r_x , r_y , and r_z are unit vectors in the x, y, and z directions, respectively, F_{et} is the tangential force, and F_{en} is the normal force.

In 2017, Danda et al. [58] introduced a predictive mechanical model for assessing force variations during bone spur grinding in a three-dimensional setting, as shown in Figure 3. This model was grounded on the specific energy of cutting and the rate of material removal. To ascertain the model's validity, they conducted experimental validations using various grinding angles and feed directions. The findings revealed that during the actual grinding of bone tissue, a noticeable oscillating force emerges in the profile. However, this force's occurrence was unrelated to whether the grinding burr was in direct contact with the bone tissue, thus having minimal influence on the calculations. The model exhibits certain merits in computing grinding efficiency and specific grinding energy. However, the model ignores the characteristics of bone materials and fails to take into account the anisotropy of bone.

$$\overrightarrow{F}_{r} = \overrightarrow{F}_{feed} + \overrightarrow{F}_{lateral} + \overrightarrow{F}_{normal} = \overrightarrow{f} \cdot \sum \overrightarrow{F}_{n} + \overrightarrow{f} \cdot \sum \overrightarrow{F}_{t} + \overrightarrow{l} \cdot \sum \overrightarrow{F}_{n} + \overrightarrow{f} \cdot \sum \overrightarrow{F}_{t} + \overrightarrow{n} \cdot \sum \overrightarrow{F}_{n} + \overrightarrow{f} \cdot \sum \overrightarrow{F}_{t}$$
(2)

In 2022, Gaziano et al. [59] employed a multiscale modeling approach tailored for elastic damage analysis to precisely delineate the macroscopic anisotropic mechanical properties of bone tissue. They utilized the finite element method to replicate the progressive failure of bone tissue under stress, enabling an examination of the brittle damage patterns occurring between bone tissue layers, as depicted in Figure 4. Numerical simulations of bone tissue under different loading conditions were performed to verify the validity of the model. In the actual analysis of bone tissue structure, it cannot be assumed to be isotropic as in conventional analysis. Bone tissue is a multilayered composite anisotropic material, and therefore, different forms of failure in different layers need to be considered. In analyzing the form of damage to the outer bone tissue, reference can be made to the quadratic Brewer-Lagace criterion, where only the three-way stress component leads to failure, which can be expressed as:

$$F_{\text{int}}\left(\sigma\right) = \left(\frac{\left\langle\sigma_{\text{rr}}\right\rangle}{S_{\text{rr}}}\right)^{2} + \left(\frac{\sigma_{\text{r\theta}}}{S_{\text{r\theta}}}\right)^{2} + \left(\frac{\sigma_{\text{rz}}}{S_{\text{rz}}}\right)^{2} \tag{3}$$

where σ_{rr} , $\sigma_{r\theta}$, and σ_{rz} are the three-way stresses, and $S_{r\theta}$ and S_{rz} are the forward tensile and shear strengths, respectively. As for the inner layer failure mode, it can be considered from both the maximum principal stress criterion and the Von Mises criterion. If the maximum principal stress criterion is considered, the expression is:

$$F_{\text{lam}}(\sigma) = \max \left\{ \frac{\max \left\{ 0, \sigma_1, \sigma_2, \sigma_3 \right\}}{S_{\text{lam}}^+}, \frac{\min \left\{ 0, \sigma_1, \sigma_2, \sigma_3 \right\}}{S_{\text{lam}}^-} \right\}$$
(4)

Consider the Von Mises criterion, the expression is:

$$F_{\text{lam}}(\sigma) = \sqrt{\frac{3}{2} \operatorname{tr}(s)^2} / S_{\text{lam}}$$
 (5)

where s is the deviation part of σ .

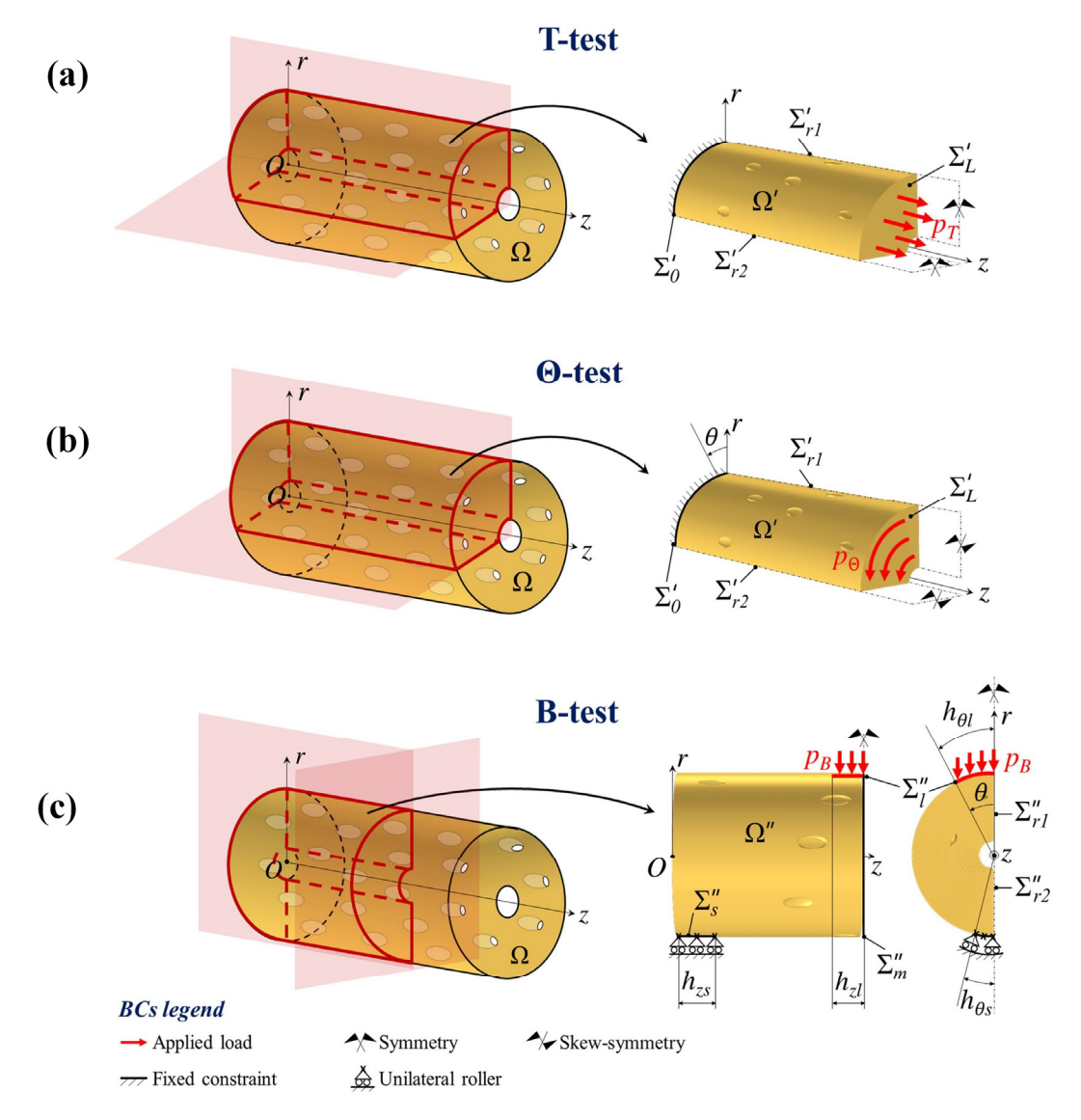


Figure 4. Anisotropic analysis of bone tissue: (a) tensile test, (b) torsion test, (c) bending test.

Sun et al. [60] proposed the asymptotic law of grinding arc length under the action of rotational ultrasound, on the basis of which they established a mathematical model for the maximum deformed chip thickness under ultrasonic vibration, as shown in Figure 5. Their findings indicate that ultrasonic vibration enhances the thickness of undeformed chips and broadens the debris removal area, thereby facilitating a reduction in grinding force. Utilizing this model, the grinding force in the x, y, and z directions can be formulated as follows:

force in the x, y, and z directions can be formulated as follows:
$$F_{x} = 2\sum_{m=1}^{L_{v}} N_{m}(m) \frac{\sin\left[\alpha_{i}(m)\right]}{\varphi_{3}} \left\{ \frac{\frac{\varphi_{i}H_{v_{u}}h_{2}^{2}\tan\theta\left(\tan^{2}\theta+2\right)^{1/2}\int_{0}^{\varphi_{i}}\sin\left[\varphi(t)\right]dt}{24} + \frac{(\varphi_{2}-\varphi_{i})\int_{\varphi_{i}}^{\varphi_{2}}\sin\left[\varphi(t)\right]dth_{2}^{16/9}\left[15l_{1}(m)+16l_{2}(m)\right]^{8/9}\tan^{14/9}\theta H_{v,s}^{4/3}K_{id}^{4/9}\left(1-v^{2}\right)^{2/9}}{(0.226^{16/9})\left[48l_{2}(m)\right]^{8/9}E^{7/9}} + \frac{(\varphi_{3}-\varphi_{2})\int_{\varphi_{2}}^{\varphi_{3}}\sin\left[\varphi(t)\right]dt}{0.678} \cdot \frac{S^{2}l_{v_{u}}(m)-h_{2}^{2}\left[l_{1}(m)+l_{2}(m)\right]}{l_{3}(m)} \cdot \frac{H_{v_{u}}^{2}\tan^{8/3}\theta}{5-4v} \cdot \left[\frac{3(1-2v)}{E} + \frac{4\sqrt{3}\cot\theta}{3\pi}\left(\frac{E}{H_{v_{u}}^{4}}\right)^{1/3}\right]}$$

$$F_{y} = 2\sum_{m=1}^{L_{c}} \frac{N_{m}(m)}{\varphi_{3}} \begin{cases} \frac{\varphi_{1}H_{v_{u}}h_{2}^{2}\left(\tan^{2}\theta + 2\right)^{1/2}\int_{0}^{\varphi_{1}}\sin\left[\varphi(t)\right]dt}{48} + \\ \frac{(\varphi_{2} - \varphi_{1})h_{2}^{2}\sin\left[\varphi(t)\right]dt\left[15l_{1}(m) + 16l_{2}(m)\right]\tan\theta H_{v_{u}}^{4/3}}{32l_{2}(m)E^{1/3}} + \\ \frac{(\varphi_{3} - \varphi_{2})\int_{\varphi_{2}}^{\varphi_{3}}\sin\left[\varphi(t)\right]dt}{0.678} \cdot \frac{S^{2}l_{c_{u}i}(m) - h_{2}^{2}\left[l_{1}(m) + l_{2}(m)\right]}{l_{3}(m)} \cdot \frac{H_{v_{u}}^{2}\tan^{8/3}\theta}{5 - 4\nu} \cdot \\ \left[\frac{3(1 - 2\nu)}{E} + \frac{4\sqrt{3}\cot\theta}{3\pi}\left(\frac{E}{H_{v_{u}}^{4}}\right)^{1/3}\right] \cdot \frac{C_{1}(m)}{C_{h}(m)} \end{cases}$$

$$(7)$$

$$F_{z} = 2\sum_{m=1}^{L_{c}} \frac{N_{m}(m)}{\varphi_{3}} \begin{cases} \frac{\varphi_{1}H_{v_{u}u}h_{2}^{2}\tan\theta\left(\tan^{2}\theta + 2\right)^{1/2}\cos\left[\alpha_{i}\left(m\right)\right]}{24} + \\ \frac{(\varphi_{2} - \varphi_{1})\cos\left[\alpha_{i}\left(m\right)\right]h_{2}^{16/9}\left[15l_{1}\left(m\right) + 16l_{2}\left(m\right)\right]^{8/9}\tan^{14/9}\theta H_{v_{u}u}^{4/3}K_{id}^{4/9}\left(1 - v^{2}\right)^{2/9}}{0.226^{16/9}\left[48l_{2}\left(m\right)\right]^{8/9}E^{7/9}} + \\ \frac{(\varphi_{3} - \varphi_{2})\cos\left[\alpha_{i}\left(m\right)\right]}{0.678} \cdot \frac{S^{2}l_{c_{u}i}\left(m\right) - h_{2}^{2}\left[l_{1}\left(m\right) + l_{2}\left(m\right)\right]}{l_{3}\left(m\right)} \cdot \frac{H_{v_{u}u}^{2}\tan^{8/3}\theta}{5 - 4v} \cdot \\ \left[\frac{3\left(1 - 2v\right)}{E} + \frac{4\sqrt{3}\cot\theta}{3\pi}\left(\frac{E}{H_{v_{u}u}^{4}}\right)^{1/3}\right] \end{cases}$$

$$(8)$$

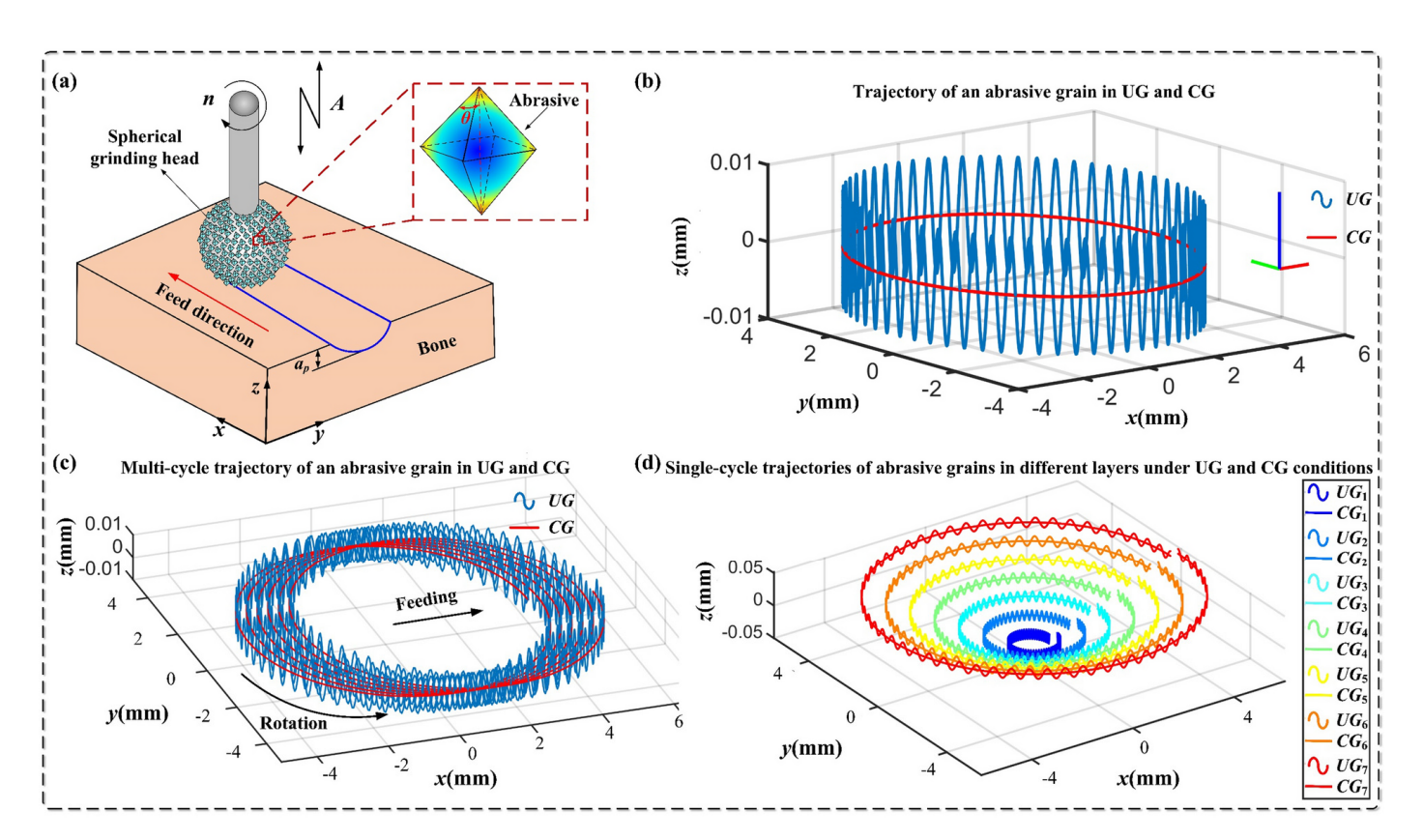


Figure 5. Ultrasonic vibratory grinding force model in Sun's study: (a) abrasive tool motion trajectory diagram, (b) abrasive grit motion trajectory, (c) abrasive grit multiaxial motion trajectory, (d) abrasive grit motion trajectory at different levels.

In 2024, Zhu et al. [61] established a finite element model for ultrasonic vibration-assisted (UVAG) grinding of cortical bone based on kinematic equations. By integrating experimental data, they establish a quadratic regression model to investigate how machining and vibration parameters influence the grinding force. Experimental findings reveal

that the grinding force initially declines and then gradually increases with an increase in amplitude. The equation used to predict the grinding force can be formulated as:

$$F = 6.64 + 0.0142v + 0.0238h - 1.624A - 0.000001v^{2} - 0.00134h^{2} + 0.05149A^{2} + 0.000209vh - 0.000157vA + 0.00390hA$$
(9)

Table 1 lists the relevant parameters and model errors of the grinding force model of biological bone tissue.

| Processing Method | Reference | Tool Type | Orientation (Relative to Bone Unit Orientation) | Model Accuracy | |
|----------------------|-----------|---------------------------------|--|-------------------|--|
| Grinding | [58] | Diamond grinding needles | Parallel, perpendicular, diagonal 30°, 60°, 90° | / | |
| | [57] | Diamond spherical grinding tool | Parallel, perpendicular, diagonal 30°, 60°, 90° | <23% | |
| | [62] | Diamond micro-grinding tool | 90° | / | |
| | [60] | Diamond spherical grinding tool | 90° | 4.12%~13.98% | |
| | [61] | Diamond spherical grinding tool | 90° | <20% | |

Table 1. Bone grinding force model.

2.3. Application of Models

Zhu et al. [63] examined the grinding forces under varying machining conditions and types of grinding wheels. The direction of machining significantly influences the grinding force, with the cross-sectional grinding force exceeding the side grinding force, which is greater than the surface grinding force. Additionally, the diamond grinding wheel produced a lower grinding force compared to the aluminum oxide grinding wheel. Zou et al. [57] analyzed the magnitudes of the three-directional grinding forces across various working conditions. Their findings revealed notable variations in these forces attributed to anisotropy. Additionally, adjustments in spindle inclination alter the grain's linear velocity, thereby influencing the grinding force.

Gaziano et al. [59] analyzed the form of failure of bone tissue stratification from the perspective of anisotropy, comparing the manifestation of bone failure and the change of force under different loading conditions, as shown in Figure 6.

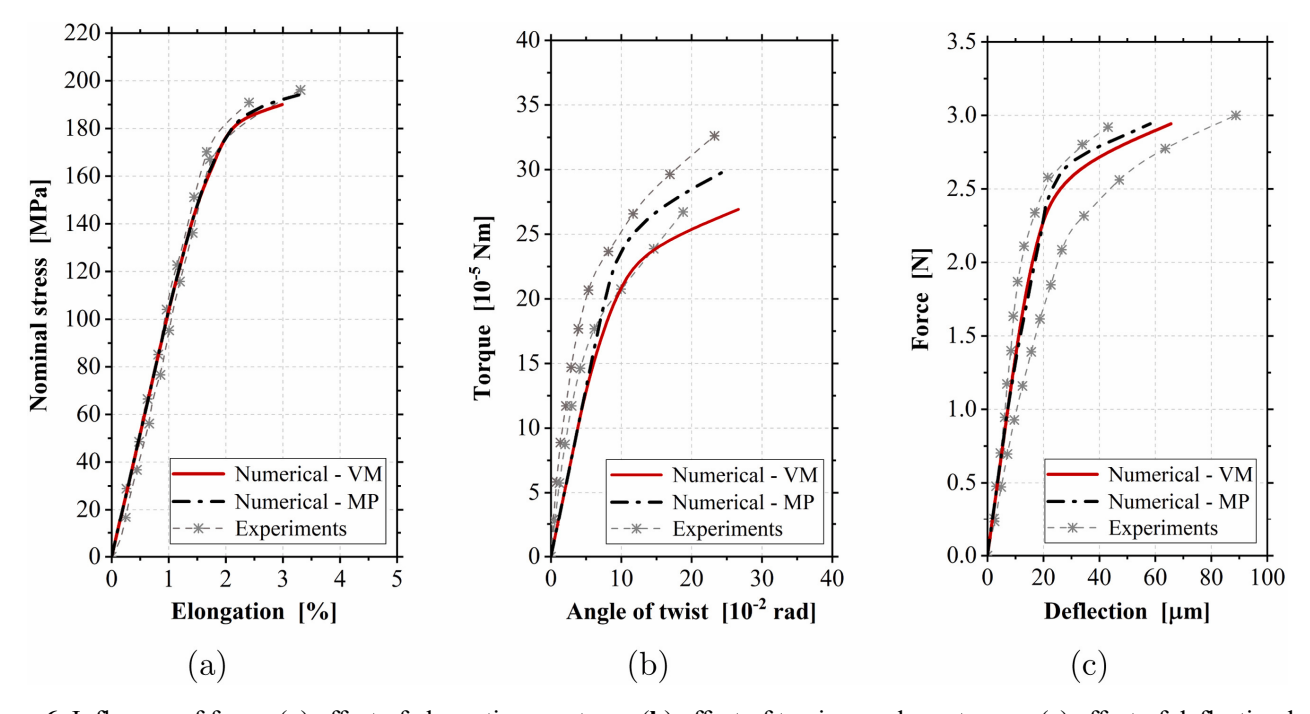


Figure 6. Influence of force: (a) effect of elongation on stress, (b) effect of torsion angle on torque, (c) effect of deflection length on cutting force.

Liao et al. [64] analyzed the chip fracture process, incorporating both dynamic and static perspectives. They experimentally gathered data on thrust and total cutting forces, varying by depth and direction during the cutting process. They also calculated three-directional milling and thrust forces, taking into account bone anisotropy [65], as depicted

in Figure 7. By examining the dynamic components of the cutting force, it is evident that the transverse cutting force's dynamic components increase significantly in the FC cutting mode, whereas they remain relatively subdued in the SC cutting mode.

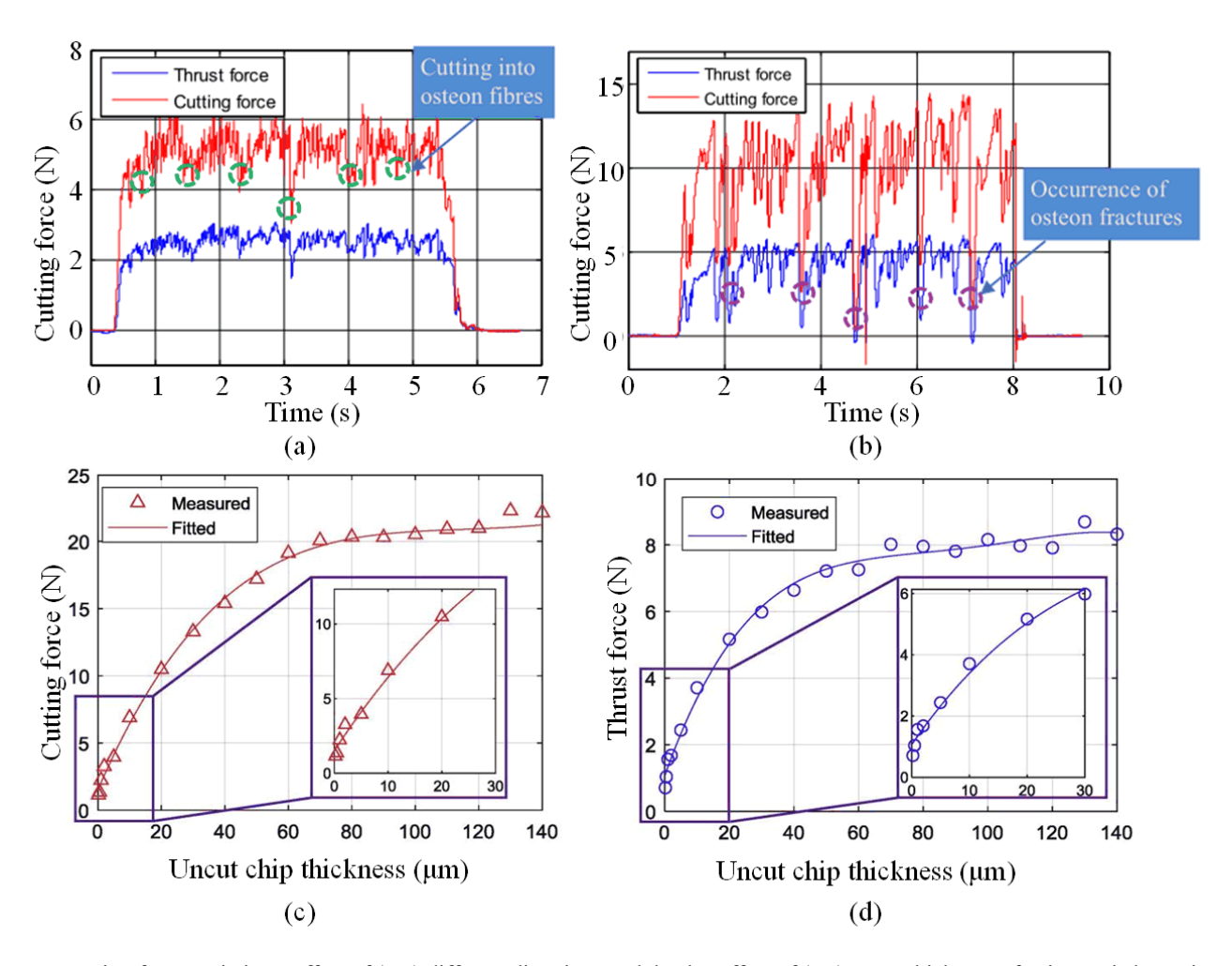


Figure 7. Cutting force variations: effect of (a,b) different directions and depths, effect of (c,d) uncut thickness of anisotropic bone tissue.

3. Biologically Inert Ceramics

3.1. Material Removal Mechanism

Bio-inert ceramic materials, such as alumina (Al₂O₃), zirconia (ZrO₂), silicon nitride (Si₃N₄), and silicon carbide (SiC), have become important materials in the biomedical field due to their excellent mechanical properties and chemical stability. The grinding processing cost of bioinert ceramics covers multiple aspects such as equipment wear and tear, tool consumption, coolant usage, labor input, and losses due to processing rejects. Among them, the grinding force plays a crucial role. A higher grinding force will accelerate tool wear, shorten tool life, and increase tool replacement costs. At the same time, it may lead to a decline in the surface quality of the workpiece and the generation of rejects, wasting raw materials and processing time and thus driving up the overall cost. By effectively controlling the grinding force through optimizing processing parameters, selecting appropriate tools and grinding fluids, etc., tool wear can be reduced, the reject rate can be decreased, and thus the processing cost can be significantly reduced, improving production efficiency and economic benefits, and realizing the cost control and optimization of bioinert ceramic cutting and grinding processing. However, during grinding processes, these ceramic materials often suffer from surface damage issues such as cracks, pits, and residual stresses [66–69]. Additionally, due to their high hardness and brittleness, ceramic materials are prone to stress concentration during processing. Unlike metals, which can absorb energy through plastic deformation when subjected to external forces from abrasive grains [70-73], ceramic materials are more likely to develop cracks or even fractures. Furthermore, the low thermal conductivity of ceramic materials makes it difficult for the heat generated during processing to dissipate quickly, leading to localized overheating and, subsequently, thermal cracks [74–76]. Therefore, analyzing the grinding mechanisms and mechanical behaviors of ceramic materials is crucial for addressing the aforementioned issues.

Ceramics are hard and brittle materials, and during grinding, plastic deformation, crack initiation, and propagation occur within the material. Accurate elaboration of these phenomena serves as a theoretical foundation for establishing ceramic grinding force models. As shown in Figure 8, during grinding, the abrasive grain and the workpiece undergo physical behaviors such as elastic deformation, plastic plowing, ductile removal, and brittle removal within the contact arc. Bifano et al. [77] found that the grinding depth of the abrasive grain on the workpiece is the primary factor influencing the material removal mechanism during grinding. When the grinding depth exceeds the critical grinding depth, the removal mechanism of brittle materials shifts to plastic removal. Yang et al. [78] observed that the removal mode in the multi-scale grinding process of ceramic materials originates from the difference in protrusion height of abrasive particles, characterized by the coexistence of ductile, brittle, and mixed removal modes. Sun et al. [79] conducted nano-scratch experiments to analyze the material removal mechanism of lithium aluminosilicate glassceramics. Based on the experimental data, they provided a more detailed definition of the critical fracture cutting depth originally described by Bifano. The results of these scratch tests revealed that as the scratch length increases and the normal load increases, the material removal process undergoes three stages, as shown in Figure 8b: elastic deformation scratch stage, plastic plowing stage, and brittle fracture stage. Zhang et al. [80] investigated the grinding force characteristics of ceramics and glasses, finding that the removal mechanism of brittle materials mainly depends on crack propagation during micro-scale grinding. Additionally, Baraheni et al. [81] established a grinding crack propagation equation for silicon nitride ceramics based on plastic deformation and brittle fracture using Vickers hardness correlation and indentation fracture mechanics theory.

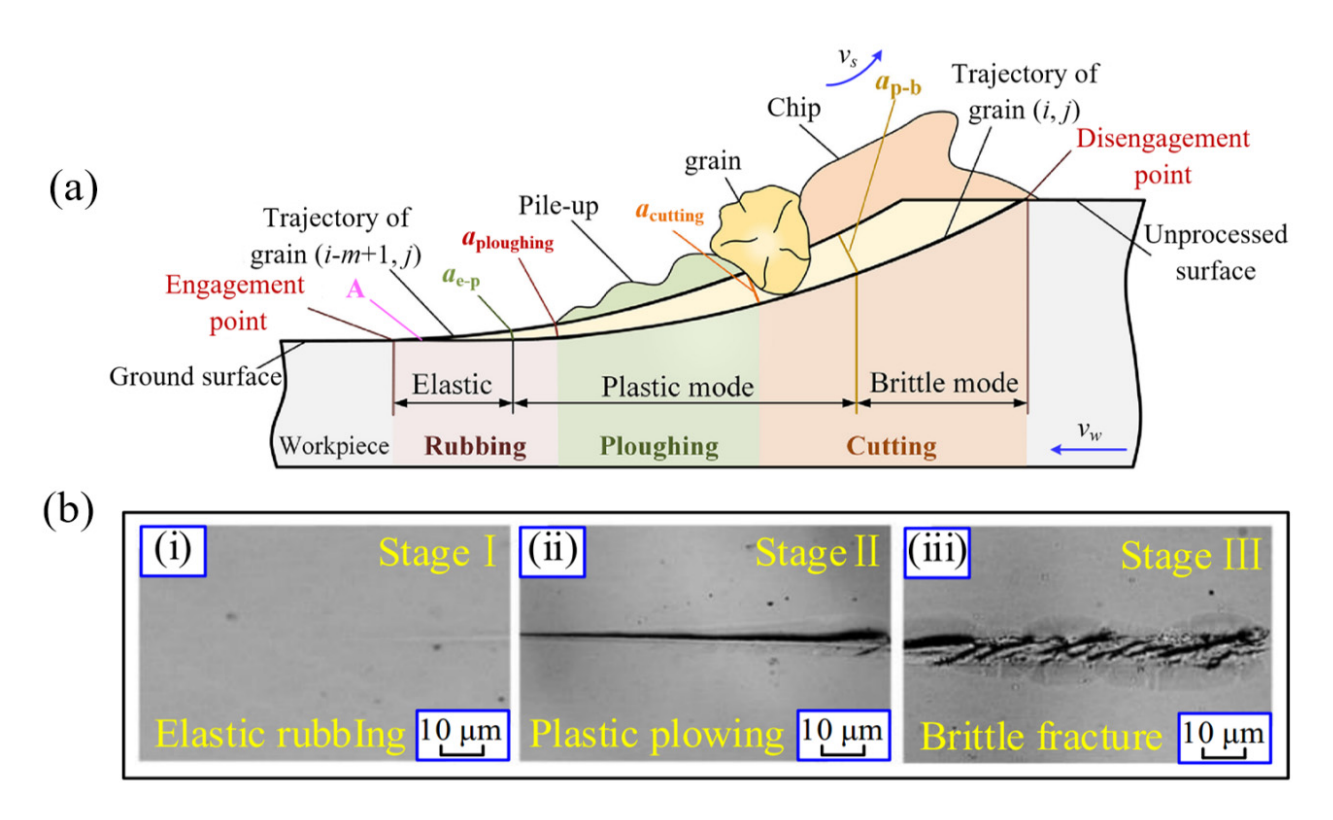


Figure 8. (a) Ceramic grinding material removal process; (b) Ceramic grinding material removal stage.

Furthermore, the grinding method also influences the material removal process in ceramics. In conventional grinding, the material ahead of the cutting edge of the abrasive grain is compressed, and chips form when the stress value exceeds the bearing limit of the ceramic material. Simultaneously, due to compressive stress and frictional heat, the material below the abrasive grain undergoes local plastic flow to form a deformed layer. After the abrasive grain passes, the deformed layer detaches from the workpiece due to the disappearance of stress, forming cutting chips. The ceramic surface may exhibit a mixture of plastic flow and fragmented chip-type damage, with obvious strip-like grinding marks, *i.e.*, intergranular fragmentation damage. Ultrasonic-assisted grinding introduces ultrasonic vibration during the grinding process to alter the trajectory of the abrasive grains. In ultrasonic-assisted grinding, the motion trajectory of the abrasive grains becomes a sinusoidal curve due to the introduction of ultrasonic vibration, making the cutting path of the abrasive grains on the workpiece more complex and further increasing the material removal rate. At the same time, the motion trajectories of adjacent abrasive grains intertwine to form a net-like grinding surface, further

improving the surface quality of the workpiece. Li et al. [82] established a theoretical model for the normal grinding force based on ultrasonic vibration-assisted grinding trajectories and scratch tests, and studied the removal mechanism of Si₃N₄ ceramics in ultrasonic vibration-assisted grinding. They found that ultrasonic vibration-assisted grinding is beneficial for improving surface quality. Qiao et al. [83] compared the cutting force, scratch morphology, and removal mode between traditional grinding and ultrasonic vibration-assisted grinding of Si₃N₄ ceramics and analyzed the removal mechanism and crack suppression effect of Si₃N₄ ceramic materials under ultrasonic vibration. They found that as the scratch spacing increases, the crack suppression effect between scratches gradually decreases.

3.2. Grinding Force Model

3.2.1. Zirconia Ceramics

In the study of conventional grinding of zirconia ceramics. Xie et al. [84] carried out a comprehensive and systematic investigation into the grinding mechanisms of high-speed deep grinding and the damage mechanisms associated with ceramic materials. They developed grinding force equations for individual abrasive particles interacting with zirconia ceramics under two distinct material removal mechanisms: plastic deformation and brittle fracture.

Grinding force of grinding process based on brittle fracture:

$$\begin{cases} F_{n'} = 2Np_{c}l_{c}h_{\text{max}} + N\left(\eta_{0}\xi \tan^{2}\theta Hh_{c}^{2} - 2p_{c}\right)l_{p}h_{c} + 2NS\overline{p}h_{\text{max}}l_{c} \\ F_{\tau'} = \frac{\pi}{2\tan\theta}Np_{c}l_{c}h_{\text{max}} + \frac{\pi}{4\tan\theta}N\times \\ \left(\eta_{0}\xi \tan^{2}\theta Hh_{c}^{2} - 2p_{c}\right)l_{p}h_{c} + 2\mu NS\overline{p}h_{\text{max}}l_{c} \end{cases}$$

$$(10)$$

Grinding force of grinding process based on plastic deformation:

$$\begin{cases} F_{n'} = \eta_0 \xi \tan^2 \theta N H h_{\text{max}}^3 l_c + 2N \overline{p} h_{\text{max}} l_c \\ F_{\tau'} = \frac{\eta_0 \pi}{4} \xi \tan^2 \theta N H h_{\text{max}}^3 l_c + 2\mu N \overline{p} h_{\text{max}} l_c \end{cases}$$

$$(11)$$

where η_0 is a constant ranging from 0 to 1; ξ is the geometric factor of the indenter, where for a Vickers indenter, $\xi = 2$; θ is the half-angle of the apex of the indenter or abrasive particle; H is the hardness of the material; N is the number of abrasive particles contained in a unit volume; S_p is the normal force exerted by a single abrasive particle due to friction force; I_c is the arc length of contact in the grinding zone. P_c is the cutting force during brittle removal in grinding processing; h_c is the critical cutting depth for ductile removal; and h_{max} is the maximum undeformed chip thickness.

Researchers have long investigated the mechanical properties of zirconia ceramics during grinding to improve machining quality. However, challenges such as the brittleness of ceramics, difficulty in machining, high tool wear, and edge breakage continue to make ceramic machining difficult [85,86]. Traditional grinding methods have proven ineffective for ceramic processing, as they rely on a shear-based cutting mechanism that leads to fracture due to the material's brittleness [87]. As a result, non-traditional assisted grinding techniques have been developed to overcome these challenges.

Xiao et al. [88] investigated the combined effects of plastic removal and brittle fracture mechanisms on the cutting force model in the Ultrasonic Vibration-Assisted Side Grinding (UVASG) process of ceramics. They proposed a theoretical cutting force model for UVASG that simultaneously considers both plastic flow removal and brittle fracture removal mechanisms. Figure 9 illustrates the schematic of UVASG. Through this model, readers can better understand the ultrasonic-assisted grinding force under the two removal modes, which is highly innovative. However, this model has not yet considered and explored the ultrasonic action modes, such as the auxiliary mode of ultrasonic vibration and multi-dimensional compound ultrasonic vibration.

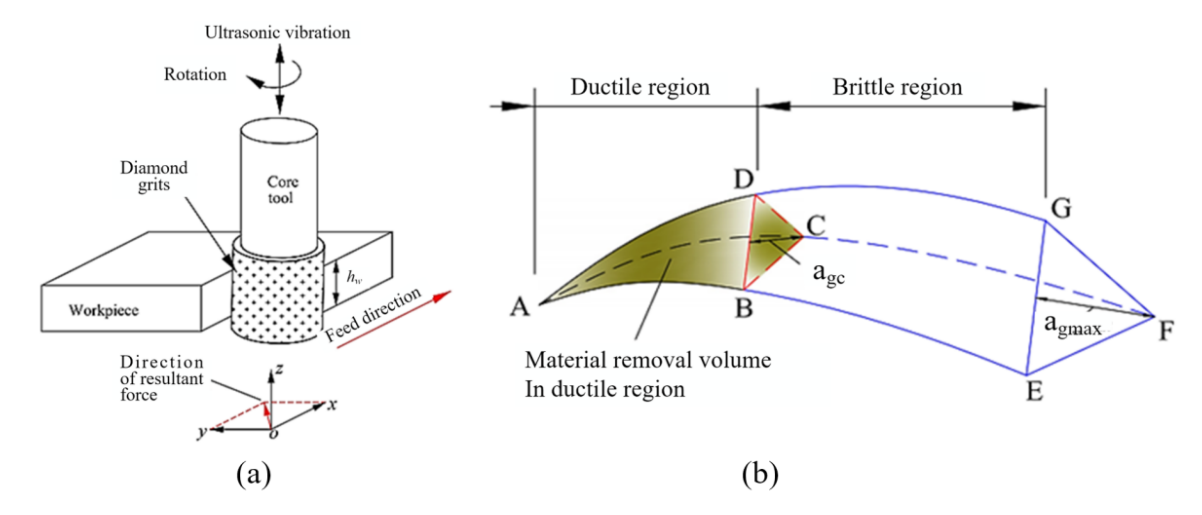


Figure 9. Schematic diagram of UVASG: (a) Schematic diagram of UVAG processing;(b) Ductile and brittle zones in UVASG. Ductile Zone Cutting Force Model:

$$F_d = N_a \cdot \frac{2}{3} a_{gc}^2 \tan \frac{\alpha}{2} \cdot \sqrt{\tan^2 \frac{\alpha}{2} + 2} \cdot H_v \tag{12}$$

Brittle Zone Cutting Force Model:

$$F_{b} = N_{a} \cdot \frac{a_{gmax}^{2}(l_{d} + l_{b}) - a_{gc}^{2}l_{d}}{6l_{b}} \xi \tan^{2} \frac{\alpha}{2} H_{v}$$
(13)

The number of active abrasive grains:

$$N_{a} = \frac{120v_{f}a_{e}h_{w} \cdot H_{v}^{3/8}K_{IC}^{1/2}(1-v^{2})^{1/4}}{2n \cdot \tan\frac{\alpha}{2}a_{aved}^{2}l_{d} \cdot H_{v}^{3/8}K_{IC}^{1/2}(1-v^{2})^{1/4} + n \cdot C_{2}^{2}\left(\tan\frac{\alpha}{2}\right)^{3/2}\xi^{9/8}E^{7/8} \cdot a_{aveb}^{9/4}l_{b}}$$
(14)

The final cutting force model for the UVASG process is:

$$F = \frac{K \cdot nN_{a}H_{v}}{60} \left(\frac{2}{3}a_{gc}^{2} \tan \frac{\alpha}{2} \cdot \sqrt{\tan^{2}\frac{\alpha}{2} + 2 \cdot t_{1} + (t_{2} - t_{1})} \cdot \frac{a_{gmax}^{2}(l_{d} + l_{b}) - a_{gc}^{2}l_{d}}{6l_{b}} \xi \tan^{2}\frac{\alpha}{2}\right)$$
(15)

where a_{gc} is the critical depth of cut, V_s is the theoretical removal rate of a single diamond abrasive grain, V_t is the total material removal rate, H_v indicates the hardness of the workpiece, ξ is the geometric factor of the indenter, a_e represents the cutting width, h_w is the contact height between the tool side and the workpiece, K_{IC} is the fracture toughness of the workpiece material, a_{aved} is the average cutting depth, a_{gmax} represents the maximum cutting depth, l_b is the trajectory length of a single diamond grain in the brittle zone, l_d is the trajectory length of a single diamond grain in the ductile zone, α is the angle between two opposing edges of the diamond abrasive grain.

On the basis of one-dimensional ultrasonic vibration, scholars have introduced two ultrasonic vibrations for assisted grinding. The surface quality of the workpiece is further improved, and the surface damage, such as roughness and cracks, is reduced [89–91]. As shown in Figure 10, two-dimensional ultrasonic vibration mainly involves coupled vibrations and includes three primary types: longitudinal-bending [92], double-bending [93], and longitudinal-torsional [94,95]. Among these techniques, longitudinal-torsional coupled ultrasonic vibration (LTC-RUM) stands out as the preferred choice for machining hard and brittle materials, primarily due to its straightforward structure and straightforward implementation process.

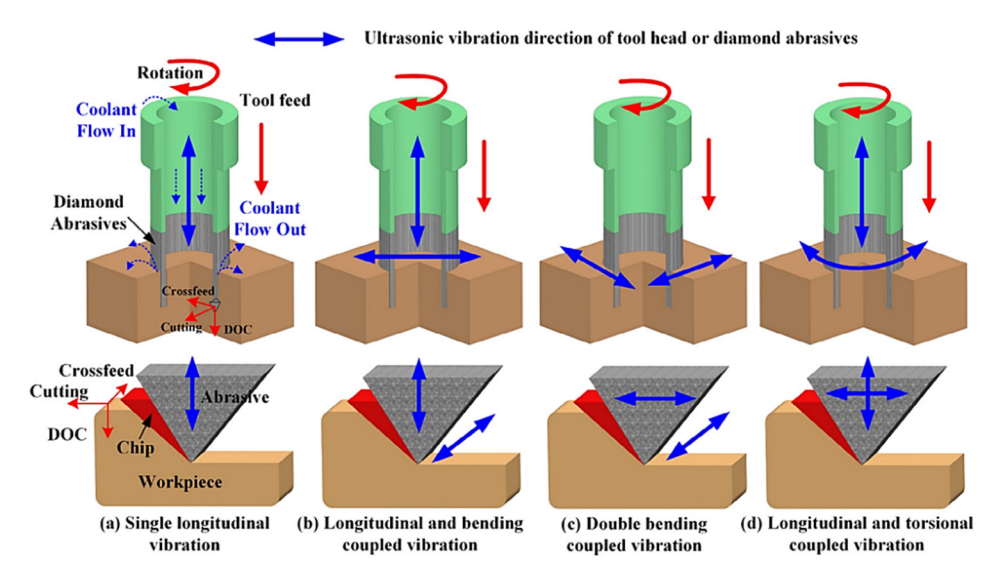


Figure 10. Ultrasonic Vibration Machining in Different Modes [96].

Researchers have extensively studied longitudinal-torsional coupled ultrasonic vibration grinding, but models related to LTC-RUM face grinding are rare. Chen et al. [97] described a cutting force model for LTC-RUM of zirconia ceramics (as shown in Equation (16)).

$$F = \left[\frac{3v_{w}H_{V}^{3/2}K_{IC}^{1/2}(1-v^{2})^{1/4}\lambda^{9/8}C_{1}^{1/8}C_{a}^{1/12}(D_{2}^{2}-D_{1}^{2})^{9/8}\left(\frac{\pi}{2}-\arcsin(1-\frac{\delta}{A_{L}})\right)^{9/8}}{4^{9/8}K_{V}f^{17/8}C_{2}^{2}E^{7/8}S_{a}^{1/4}(\cot\psi)^{3/4}\left(A_{T}\sin(2\lambda(\frac{\pi}{2}-\arcsin(1-\frac{\delta}{A_{L}}))+\frac{\lambda Rn}{30f}\left(\frac{\pi}{2}-\arcsin(1-\frac{\delta}{A_{L}})\right)\right)} \right]^{8/9}$$
(16)

where $\psi = 45^{\circ}$ represents the half-angle at the tip of the abrasive grain, λ is the proportional coefficient, C_a denotes the concentration of abrasive grains, S_a is the abrasive grain size.

The cutting process of zirconia ceramics includes both ductile and brittle phases. Bie et al. [98] examined the motion of individual abrasive grains, cutting depth, and material removal rate corresponding to each phase. They developed a cutting force model for the end-face grinding of zirconia ceramics using LTC-RUM, which considers both the ductile and brittle phases of material removal. This model can predict the grinding force relatively accurately. However, during the establishment process, some variable conditions were assumed and simplified in a rather idealized way (for example, all abrasive particles are spherical, of the same size and completely rigid, and the impact of abrasive particles on the cutting force on the peripheral surface of the cutting tool was ignored, *etc.*). In the actual grinding process, these variable conditions are uncontrollable.

The number of active abrasive particles in end-face grinding:

$$N = \frac{2(d_{o} + d_{i})h_{e}v_{w}K_{C}^{3/4}}{NfK_{C}^{3/4}(D_{2}^{2} - D_{1}^{2})\left(r_{g}^{2}\cos\left(1 - \frac{h_{d-ave}}{r_{g}}\right) - \left(r_{g} - h_{d-ave}\right)\sqrt{2r_{g} - h_{d-ave}^{2}}\right)L_{df} + 2NfK_{V}F_{bs}^{3/4}\left(2r_{g}h_{b-ave} - h_{b-ave}^{2}\right)^{1/2}L_{bf}}$$
(17)

By calculating the average cutting forces associated with each mode, the final cutting force is obtained:

$$F = \frac{4NE\left(\left(2r_{g}h_{d-ave} - h_{d-ave}^{2}\right)^{\frac{3}{2}}L_{df} + r_{g}^{\frac{3}{2}}h_{b-ave}^{\frac{3}{2}}L_{bf}\right)}{3r_{g}\left(1 - v^{2}\right)L}$$
(18)

where K_C is the fracture toughness; K_d represents the dynamic fracture toughness; $h_{d\text{-}ave}$ is the average indentation depth; K_V is the crack volume coefficient.

3.2.2. Alumina Ceramic

Xie et al. [99] performed deep grinding experiments and measured the grinding force, finding that alumina ceramics mainly undergo brittle removal. Based on this, they derived an average grinding force formula for individual abrasive grains.

$$F_{n} = \frac{(\sin\theta \cdot F_{x} + \cos\theta \cdot F_{z})\sqrt{d_{s} - a_{e}}}{C\omega b\sqrt{d_{s}}}$$

$$F_{\tau} = \frac{(\sin\theta \cdot F_{z} - \cos\theta \cdot F_{x})\sqrt{d_{s} - a_{e}}}{C\omega b\sqrt{d_{s}}}$$
(19)

Later, Xie et al. [84] expanded upon this model to further explore the mechanisms involved in high-speed deep grinding and ceramic material damage, ultimately establishing a model for the grinding force in engineering ceramics.

$$\begin{cases} F_{n} = 2Np_{c}l_{c}h_{\text{max}} + N(\eta_{0}\xi \tan^{2}\theta Hh_{c}^{2} - 2p_{c})l_{p}h_{c} + 2NS\overline{p}h_{\text{max}}l_{c} \\ F_{\tau} = \frac{\pi}{2\tan\theta}Np_{c}l_{c}h_{\text{max}} + \frac{\pi}{4\tan\theta}N\times\left(\eta_{0}\xi \tan^{2}\theta Hh_{c}^{2} - 2p_{c}\right)l_{p}h_{c} + 2\mu NS\overline{p}h_{\text{max}}l_{c} \end{cases}$$

$$(20)$$

In the process of studying the grinding force of conventional grinding of alumina ceramics, in addition to adjusting the size of the grinding force by changing the grinding parameters, the shape of the grinding wheel and the difference of the grinding surface pattern also has a great influence on the grinding force. Wu et al. [100] developed a new brazed diamond end-face grinding wheel with micro-textured aligned grains for precise grinding of hard-brittle materials. Using a laser to ablate micro-grooves and micro-pores on the diamond abrasive surface, they applied this micro-textured brazed diamond grinding wheel to alumina ceramics and developed a grinding force model based on measured grinding forces. The workpiece is subjected to two force components, F_t and F_v , as shown in Figure 11.

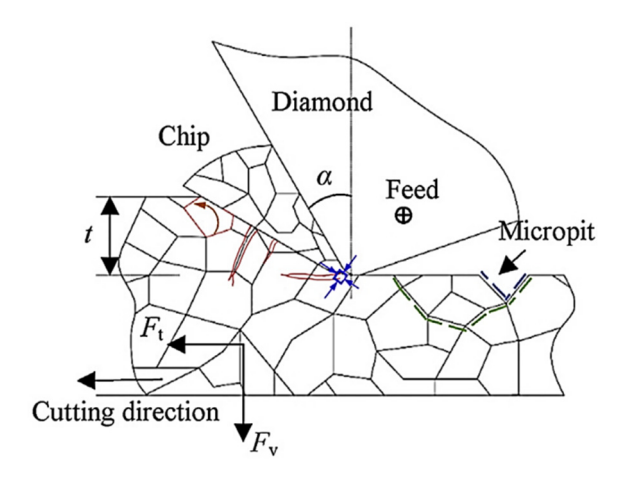


Figure 11. Geometric Model of Abrasive Particles—Orthogonal Cutting Geometric View.

The relationship between F_v , F_r and F_z :

$$\begin{cases} F_r = F_v \sin \gamma \\ F_z = F_v \cos \gamma \end{cases} \tag{21}$$

When the rotation angle is θ , the diamond grains are subjected to the three-dimensional forces F_t , F_r , and F_z :

$$\begin{cases} F_x(\theta) = -F_r \sin \theta - F_t \cos \theta \\ F_y(\theta) = F_r \cos \theta - F_t \sin \theta \\ F_z = F_z \end{cases}$$
 (22)

k diamond particles cut into the workpiece at different positions, exerting forces in the x, y, and z directions.

$$F_{s} = \sum_{i=1}^{k} F_{is}(s = x, y, orz)$$
 (23)

The application of ultrasonic-assisted grinding technology in the processing of alumina ceramics has made

remarkable progress in recent years. Zhao et al. [32] studied longitudinal UVAG of alumina ceramics. By combining the kinematic theory of longitudinal UVAG with the effective cutting trajectory of a transient single abrasive grain and transient material removal, they developed a grinding force model and end-face grinding force model for longitudinal UVAG of alumina ceramics (shown in Figure 12).

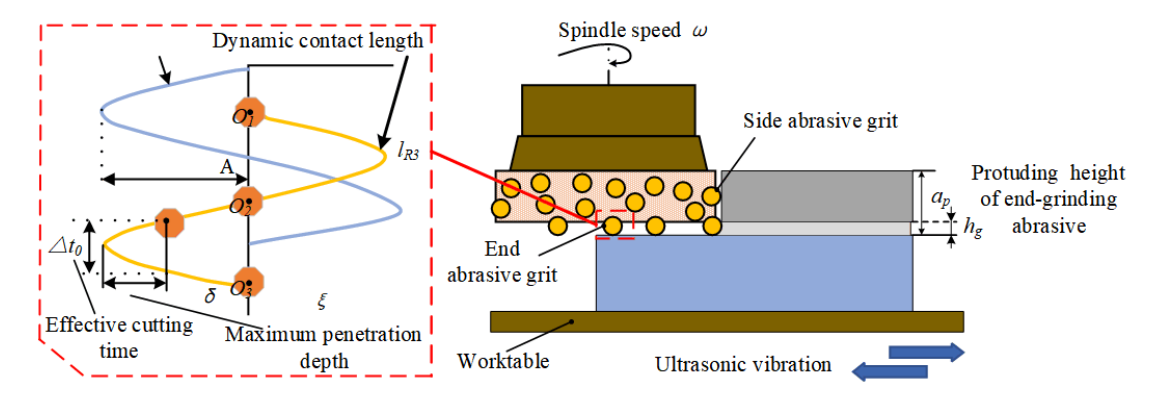


Figure 12. Effective cutting path of a single abrasive particle in longitudinal ultrasonic vibration-assisted end grinding.

Tangential and normal components of end face grinding force:

$$\begin{cases}
F_{n} = \left(\frac{c_{4}^{1/2}c_{5}^{8/9}c_{6}\left(K_{l}C^{*}\right)^{2/3}H^{1/2}v_{w}^{2}}{\sqrt{a_{p}R\left[\left(v_{s}\right)^{2}+\left(4Af\right)^{2}\right]}}\right)^{6/7} \\
F_{\tau} = \zeta \left(\frac{c_{4}^{1/2}c_{5}^{8/9}c_{6}\left(K_{l}C^{*}\right)^{2/3}H^{1/2}v_{w}^{2}}{\sqrt{a_{p}R\left[\left(v_{s}\right)^{2}+\left(4Af\right)^{2}\right]}}\right)^{6/7}
\end{cases} (24)$$

Longitudinal UVAG grinding force model:

$$\begin{cases}
F_{n} = \left(\frac{C\pi\theta R_{s}^{3/2} a_{p}^{3/2} n_{s}}{A v_{s}}\right) + \left(c_{1} \frac{c_{a}^{2/3}}{s^{2}} \sqrt{\frac{a_{p}}{R_{s}}} \frac{v_{w}}{v_{s}}\right) + \left(\frac{c_{4}^{1/2} c_{5}^{8/9} c_{6} \left(K_{I} C^{*}\right)^{2/3} H^{1/2} v_{w}^{2}}{\sqrt{2\pi n_{s} R \left[\left(v_{s}\right)^{2} + \left(4Af\right)^{2}\right]}}\right)^{6/7} \\
F_{\tau} = \left(\frac{CC_{1} \pi \theta R_{s}^{3/2} a_{p}^{3/2} n_{s}}{A v_{s}}\right) + \left(c_{2} \frac{c_{a}^{2/3} R_{s}}{s^{2}} \sqrt{\frac{a_{p}}{R_{s}}} + c_{3} \frac{c_{a}^{2/3}}{s^{2}} \sqrt{\frac{a_{p}}{R_{s}}} \frac{v_{w}}{v_{s}}\right) + \\
\zeta \left(\frac{c_{4}^{1/2} c_{5}^{8/9} c_{6} \left(K_{I} C^{*}\right)^{2/3} H^{1/2} v_{w}^{2}}{\sqrt{2\pi n_{s} R \left[\left(v_{s}\right)^{2} + \left(4Af\right)^{2}\right]}}\right)^{6}
\end{cases} \tag{25}$$

3.2.3. Silicon Nitride Ceramics

Fu et al. [101] tackled the intricacies and imprecision of current surface roughness (Ra) prediction models by introducing a novel prediction model specifically for Si_3N_4 ceramics, formulated from a frequency domain viewpoint and grounded in a dynamic grinding force framework (as shown in Figure 13). This model has fully quantified the characteristics of the grinding wheel, including abrasive wear, quantity distribution, and the undulation height of single grains. However, it ignores the thermal deformation, elastic deformation, and grinding heat effect between the grinding wheel particles and the materials.

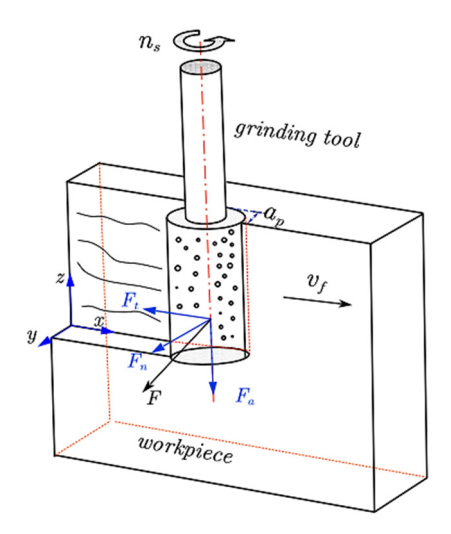


Figure 13. Grinding schematic diagram.

Dynamic grinding force model:

$$F_{D} = \frac{e^{-h_{\min}^{2}/2\sigma^{2}} \pi d_{s}b\lambda_{2} n_{s} \left(2\pi n_{s} v_{w} (1+\mu^{2})\right)^{\frac{1}{2}}}{120 \left(h_{w} + a_{g \max}\right)^{\frac{1}{2}}} \times \left[\left(\frac{2K_{IC}^{\frac{3}{4}} H^{\frac{1}{2}}}{k_{1} k_{2}} \frac{(\pi v_{w} n_{s})^{\frac{1}{2}} \tan \alpha \left(2h_{w} a_{ghi} + a_{ghi}^{2}\right)(t_{2} - t_{1})}{(2h_{w} + 2a_{g \max})^{\frac{1}{2}}} \right]^{\frac{4}{5}} + \zeta H a_{ghi}^{2} \tan^{2} \alpha$$

$$(26)$$

3.2.4. Silicon Carbide Ceramics

Cao et al. [102] developed predictive models for normal and tangential forces in UVAG of silicon carbide ceramics. Their analysis focused on the length of uncut chips generated by the relative motion between the grinding wheel and the workpiece, as well as the cutting action of individual active grains. The relative motion between the grinding wheel and the workpiece is shown in Figure 14.

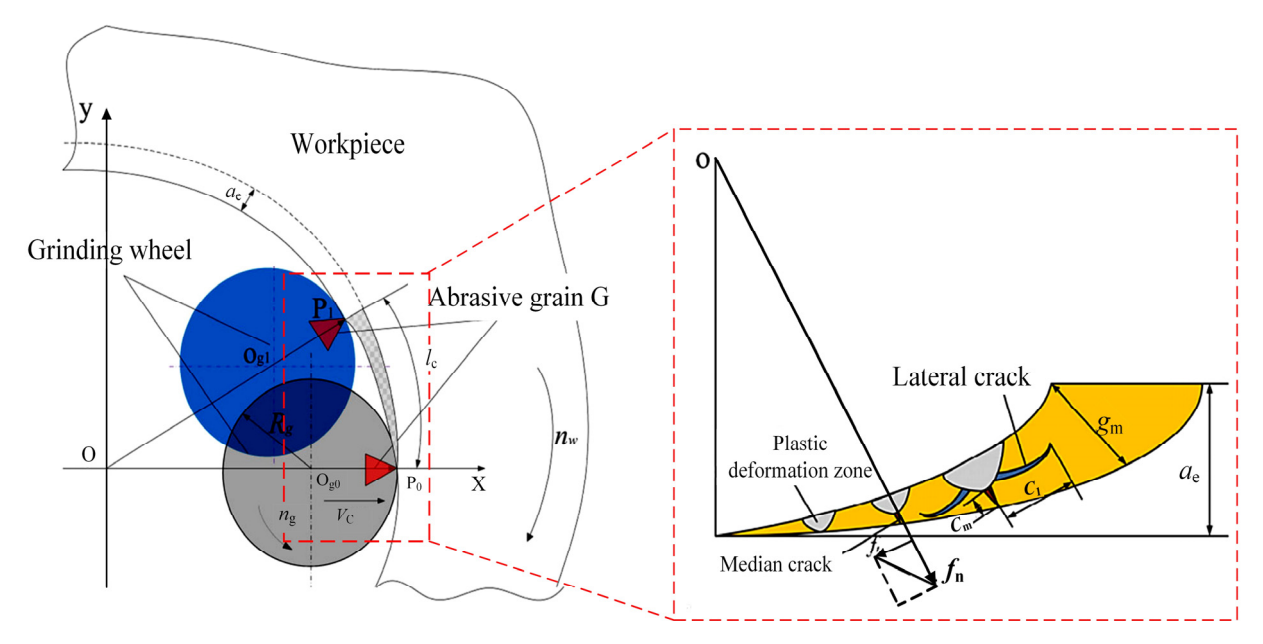


Figure 14. Relative motion between grinding wheel and workpiece.

$$\begin{cases}
F_{\tau} = k_{1}k \sqrt{\frac{2R_{w}a_{p}}{1 - R_{g} / (R_{w0} + V_{c}t_{0})}} \frac{b(R_{w0} + V_{w}t_{0})a_{p}n_{w}}{R_{g}nL_{c-UAIG}} \frac{1}{\Delta t} \int_{t_{0}}^{t_{0} + \Delta t} \cos\theta dt \\
F_{n} = k \sqrt{\frac{2R_{w}a_{p}}{1 - R_{g} / (R_{w0} + V_{c}t_{0})}} \frac{b(R_{w0} + V_{w}t_{0})a_{p}n_{w}}{R_{g}nL_{c-UAIG}}
\end{cases} (27)$$

where R_g represents the wheel radius, R_w is the workpiece radius.

Ye et al. [103] combining theories on material removal characteristics of silicon carbide ceramics, grinding principles, and brittle material fracture mechanics, developed a cutting force prediction model for longitudinal torsional ultrasonic vibration grinding of SiC ceramics.

$$F = K \cdot \left[\frac{H^{35} \cdot K_{IC}^{12} \cdot (1 - v^2)^6 \cdot C_a^{4/3} \cdot v_c^{24} \cdot a_e^{24} \cdot a_p^{24}}{\xi \cdot \cot^{17}(\alpha_0 / 2) \cdot E^{21} \cdot S_a^4 \cdot A^2 \cdot n^{24} \cdot r^{24}} \right]^{1/26}$$
(28)

Table 2 presents the categories of cutting force models along with their associated errors for diverse types of bioinert ceramics, categorized according to various machining techniques.

| Workpiece Material | Machining Methods | References Model Categories | | Error | | |
|-----------------------|---|--|---|--------|--|--|
| | | [0.41 | Cutting force model under plastic deformation. | | | |
| | | [84] | Cutting force model for under brittle fracture. | / | | |
| | | [88] | Considering both plastic flow removal and brittle fracture removal. | 14.40% | | |
| | Conventional | [97] Grinding force model under longitudinal-torsiona coupling. | | 16% | | |
| Zirconia ceramics | | [98] Grinding force model incorporating both ductile and brittle phases. | | 6.975% | | |
| | | [100] | Grinding force model for micro-textured diamond grinding wheels. | / | | |
| | | [99] | Unit grinding force model for grinding wheels in high- | / | | |
| | | [84] | speed deep grinding. | / | | |
| | Ultrasonically Assisted [104] | | Single particle grinding force model under two- dimensional ultrasonic vibration. | | | |
| Silicon nitride | Conventional [101] Ultrasonically Assisted [103] | | Dynamic grinding force model for single crystal grain scratch based on ductile-brittle removal. | 19.51% | | |
| ceramics | | | Longitudinal-torsional ultrasonic vibration grinding force model based on brittle fracture. | <15% | | |

Table 2. Mechanical model of bio-inert ceramics.

3.3. Application of Models

The force models of bioinert ceramics are essential in the design and manufacturing of medical devices. The force model helps assess the mechanical characteristics of materials under physiological conditions, guaranteeing their robustness and longevity, thereby boosting the safety and efficiency of implants.

3.3.1. Zirconia Ceramics

Xie et al. [84] conducted experimental validations of the grinding force equations corresponding to the two material removal mechanisms—plastic deformation and brittle fracture—during zirconia ceramic grinding. The results show that the grinding force increases with the increase of the grinding depth and the feed rate, whereas it diminishes as the wheel speed accelerates. Additionally, the influence of grinding parameters on the plastic cutting force is more significant compared to their impact on the brittle fracture cutting force. Xiao et al. [88] formulated a theoretical cutting force model for ultrasonic vibration-assisted lateral grinding of ceramics, encompassing both plastic flow and brittle fracture removal mechanisms. This model demonstrates a direct correlation between grinding force and feed rate as well as cutting width and an inverse relationship with spindle speed (as depicted in Figure 15). An increase in vibration

amplitude leads to a reduction in cutting force, whereas the vibration frequency exhibits a negligible influence.

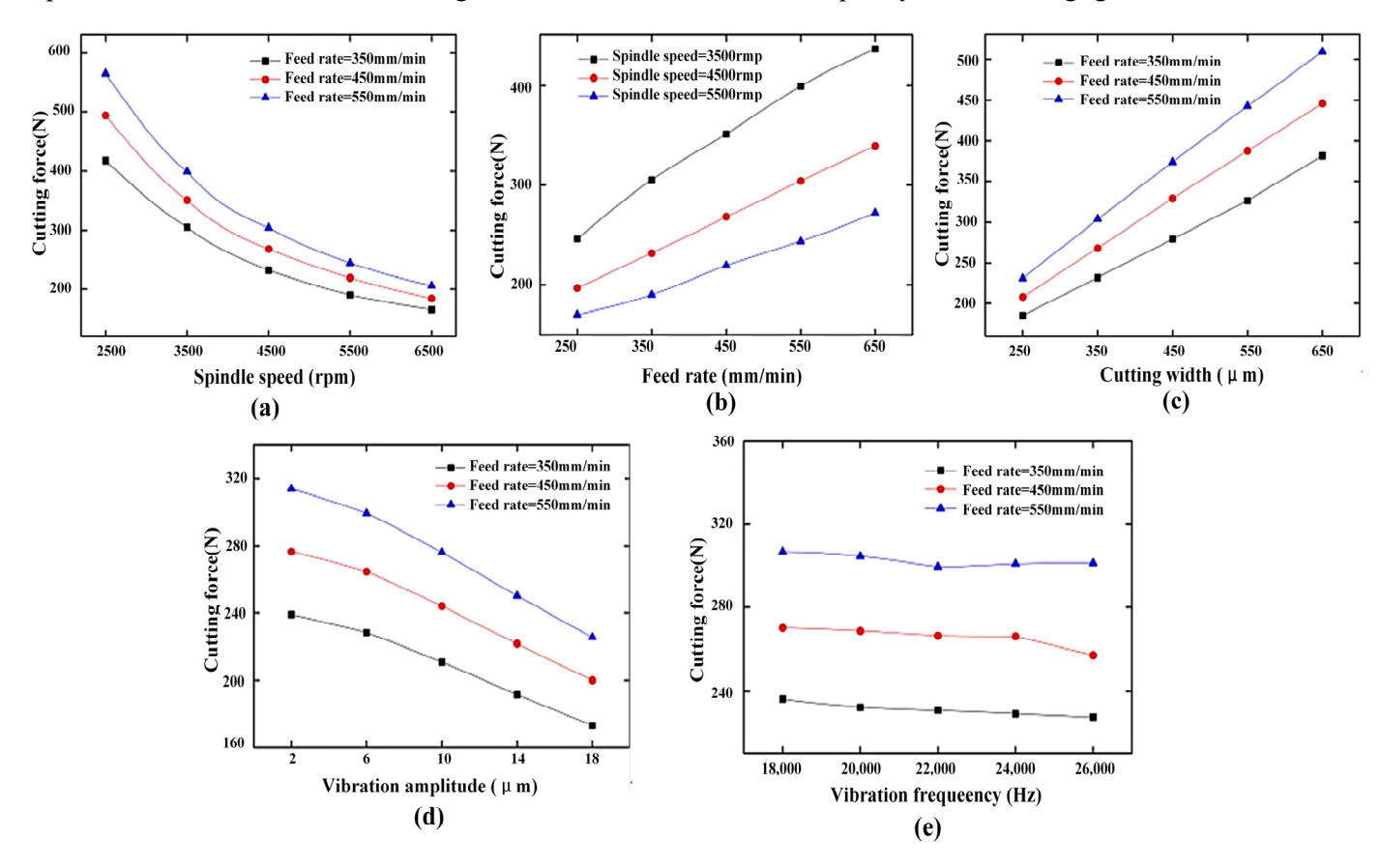


Figure 15. Predicted the relationship between cutting force and input variables: (a) the relationship between Spindle speed and Cutting force, (b) the relationship between Feed rate and Cutting force, (c) the relationship between Cutting width and Cutting force, (d) the relationship between Vibration amplitude and Cutting force, (e) the relationship between Vibration frequeecy and Cutting force.

Chen et al. [97] validated a proposed cutting force model for LTC-RUM of zirconia ceramics, finding a maximum deviation of less than 16% between predicted and experimental results. Figure 16 shows that spindle speed and ultrasonic power reduce cutting force, while feed rate increases it. Spindle speed and feed rate have a more significant impact than ultrasonic power.

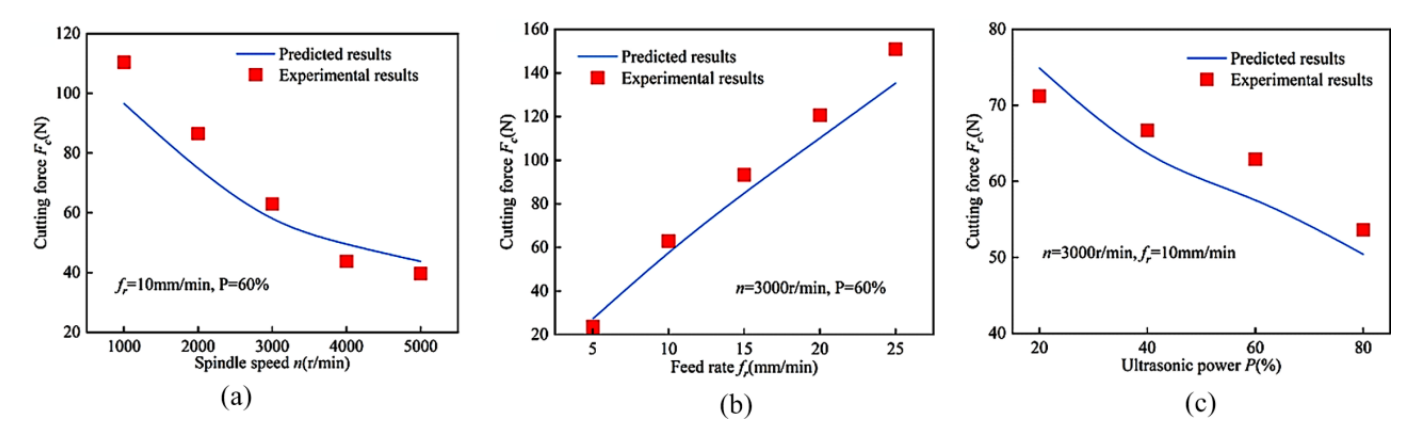


Figure 16. The relationship between machining parameters and cutting force variations: (a) spindle speed; (b) feed rate; (c) ultrasonic power.

Bie et al. [98] experimentally verified the proposed integrated cutting force model for single abrasive material removal mechanism and cutting force considering the ductile and brittle phases that exist in the cutting process of zirconia ceramics, as well as explored the relationship between various machining parameters and the experimental and predicted cutting forces. As shown in Figure 17, the predicted cutting force aligns with experimental results, decreasing with increasing spindle speed and ultrasonic power and increasing with feed rate and cutting depth.

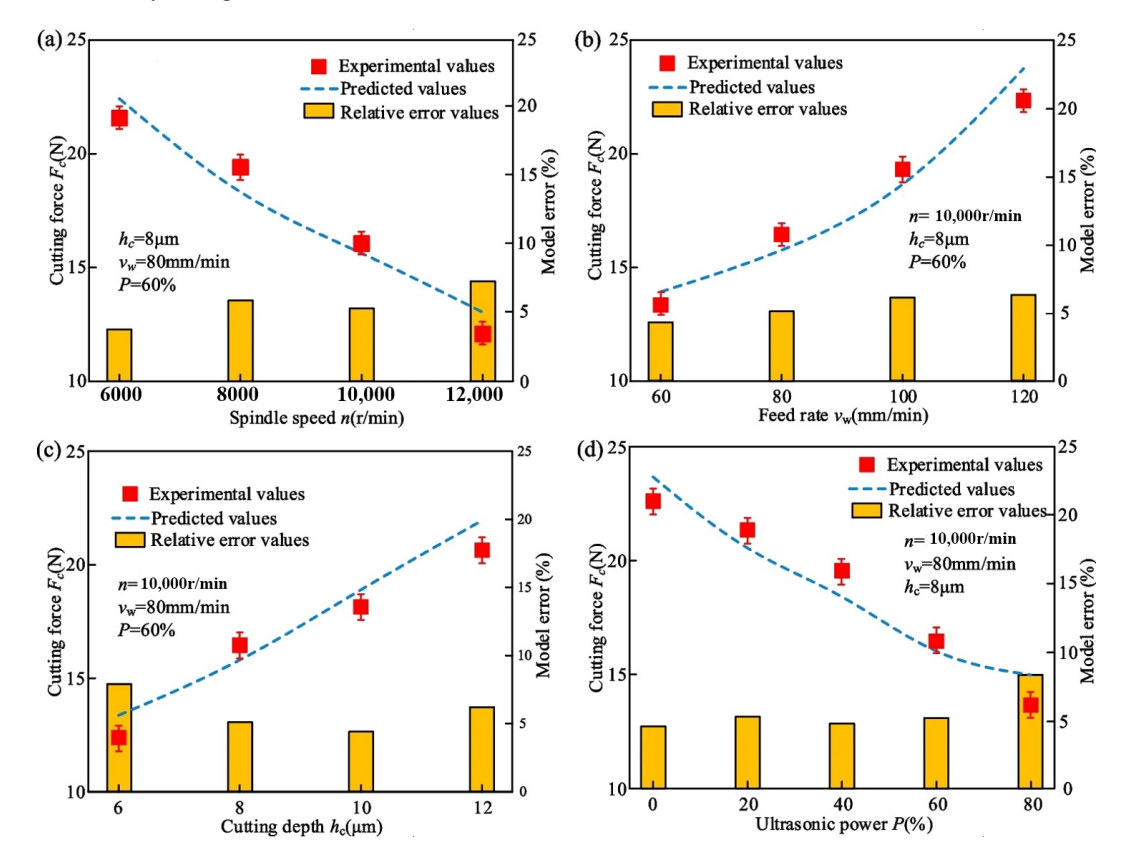


Figure 17. The relationship between the predicted and experimental cutting force and different machining parameters: (a) spindle speed, (b) feed rate, (c) cutting depth, (d) ultrasonic power.

3.3.2. Alumina Ceramic

Xie et al. [99] verified a formula for calculating the average grinding force of abrasive grains during efficient deep grinding of ceramics. The results show that the average grinding force of the abrasive grains decreases with the increase of the grinding wheel speed but increases with the increase of the grinding depth. In 2011, Xie et al. [84] proposed a grinding force model for high-speed deep grinding of alumina ceramics. Their experiments demonstrated that the grinding force decreased with higher wheel speeds and lower feed rates or grinding depths.

Cheng et al. [105] employed a micro-drilling grinding force model, utilizing undeformed chip thickness as a benchmark, to perform micro-drilling experiments on alumina ceramics. They examined the fluctuations in grinding force and its amplitude across various feed rates. The experimental results indicated that when the axial feed is set to $50 \, \mu m$, the vertical feed rate is $6 \, mm/min$, and the spindle speed is approximately $3000 \, r/min$, the grinding force remains relatively low and stable, whereas the amplitude continues to rise. The comparison of experimental data with the model revealed consistency, as illustrated in Figure 18.

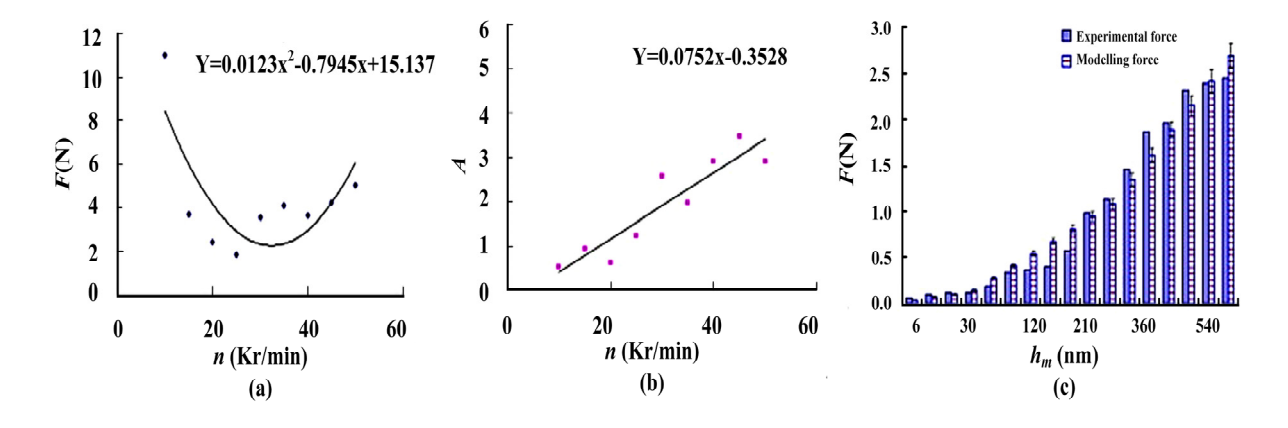


Figure 18. Micro-drill grinding force change diagram: (a) The relationship between Spindle speed and Cutting force, (b) The relationship between Spindle Speed and Vibration amplitude, (c) The relationship between Cutting depth and Cutting force.

3.3.3. Silicon Nitride Ceramics

Sun et al. [106] investigated the removal mechanisms of silicon nitride ceramics under high-speed grinding through internal surface grinding experiments on ceramics. The results presented that increasing wheel speed and reducing grinding depth effectively lower grinding force and improve surface quality. Compared to grinding depth, grinding speed has a more significant impact on both the grinding force and surface quality of the workpiece. Among them, as the grinding wheel speed increases from 55 m/s to 60 m/s, the grinding force fluctuates significantly. Through analysis, it is found that the fluctuations in the change of the grinding force are closely related to brittle fracture, and the factor of brittle fracture has a great impact on the surface morphology of the material.

Fu et al. [101] utilizing a genetic algorithm to optimize model parameters. The average relative error between the experimental and theoretical values was 19.51%, with an average grinding force error of 9.37%. The predicted error ranges for F_D and F_a are shown in Figure 19, with F_D ranging from 15.90% to 24.96% and an average of 19.51%, while F_a ranges from 3.46% to 11.93%, with an average of 8.69%.

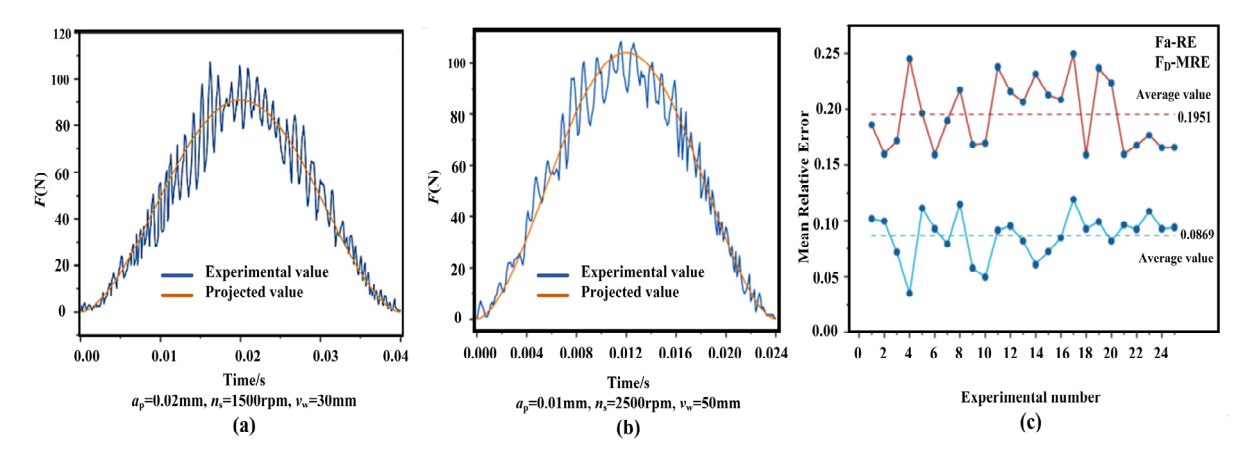


Figure 19. Research results (a), (b) comparison of theoretical prediction results; (c) Prediction error of dynamic grinding force model.

3.3.4. Silicon Carbide Ceramics

Li et al. [107] validated a micro-grinding force model tailored for silicon nitride ceramics, incorporating factors such as random abrasive distribution, grinding trajectories, and various deformation stages of materials. Their analysis showed that plowing and fracturing are the primary removal mechanisms, with model predictions closely matching experimental findings. The average deviations for normal and tangential forces were 6.793% and 8.926%, respectively. Additional experiments were conducted to investigate the relationships among grinding depth, grinding speed, and feed rate, as illustrated in Figure 20. The results indicated a linear positive correlation between cutting depth and grinding force, where the grinding force increases with increasing cutting depth. As the feed rate rises, the grinding force also increases, whereas an increase in wheel speed leads to a gradual decrease in grinding force.

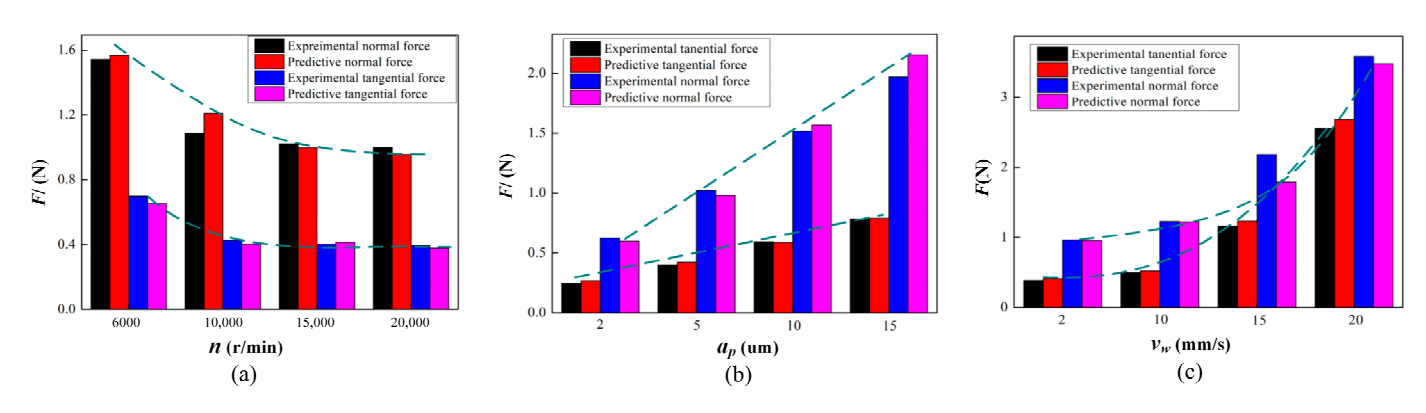


Figure 20. The relationship between grinding force with (a) grinding depth, (b) grinding speed and (c) feed speed.

Table 3 present the impacts of processing parameters on cutting force, respectively, for various types of biocompatible inert ceramics when subjected to different machining methods.

Table 3. Relationship between bio-inert ceramics and cutting force.

| Machining | Workpiece Material | References | Processing Parameters | | | | | | | | |
|-----------|--------------------------|------------|-----------------------|------------------------|------------------|-------|------------------|-------|---------------------------------------|--|--|
| Methods | | | $v_{\rm S}$ | $v_{ m W}$ | a_{p} | n | \boldsymbol{A} | f | Tool | Influence | |
| | iviatei iai | | m/s | mm/min | /mm | r∕min | /µm | /kHz | | | |
| | | [84] | 160 | 2400 | 1 | _ | | | resin bond diamond | | |
| | | | 120 | 1200 | 1 | / | / | / | grinding wheel | | |
| | | | 120 | 5000 | 0.5 | | | | grinding wheel | _ | |
| | Zirconia | [88] | / | 300 | 150 | 2800 | 5 | 20.5 | / | _ | |
| | ceramics | [97] | / | 10 | / | 3000 | 5 | 35.16 | #60~80 diamond core grinding head | Grinding forces F_n and F_t decrease with the increase of v_s , while they increase with greater | |
| | | [98] | / | 80 | 8 | 7000 | 30 | 35.32 | #60~80 diamond core grinding head | values a_p and v_w | |
| | Alumina Ceramic | [99] | 40 | 1200 | 1 | / | / | / | 120/140#resin bonded | | |
| Grinding | | | | | | | | | diamond grinding wheel | _ | |
| | | [84] | 80 | 3 mm/min ⁻¹ | 1 | / | / | / | resin bond diamond grinding wheel | | |
| | | | | 300 | 0.01 | 2500 | 2500 | | resin bond diamond grinding wheel | Grinding forces F_n and F_t decrease with the | |
| _ | Silicon nitride ceramics | | / | 180 | 0.02 | 1500 | / | / | | increase of v_s , and increase with the increase of | |
| | | | | 300 | 0.005 | 3500 | 500 | | | ap and $v_{\rm w}$. | |
| | | [106] | 0.4 | / | 4 | / | / | / | 240#resin bond diamond grinding wheel | The grinding force is proportional to the grinding depth, though the rate of increase is gradual and stable. | |
| | Silicon carbide ceramics | [107] | 2 | 3 | 2 | / | / | / | resin bond diamond grinding wheel | | |

4. Biological Alloys

4.1. Material Removal Mechanism

Titanium alloys and magnesium alloys are commonly used alloy materials in the field of bone replacement. During the cutting and grinding process of bioalloys (such as titanium alloys, etc.), the cost composition is rather complex, involving several key parts such as the depreciation and wear of equipment, the frequent replacement of cutting tools, the consumption expenditure of grinding fluid, the labor input of personnel, and the losses caused by rejects due to processing errors. The grinding force plays a vital role in this process. When the grinding force is at a relatively high level, the cutting tool will suffer more severe wear, and its durability will be greatly reduced, resulting in a significant increase in the frequency of tool replacement, directly raising the tool procurement and maintenance costs. At the same time, it is also very likely to cause defects such as scratches and burns on the surface of the workpiece, making it difficult for the product quality to meet the standards and turning into rejects. This not only causes the unnecessary waste of precious raw materials but also consumes a large amount of processing time and energy, ultimately leading to a continuous increase in the overall cost. Conversely, if the grinding force is controlled within a reasonable range through methods such as precise adjustment of grinding parameters, careful selection of suitable tool materials, and optimization of the grinding fluid formula, the tool wear rate can be effectively reduced. This, in turn, decreases the likelihood of rejects and enables better control and optimization of the cutting and grinding costs of bioalloys, significantly enhancing both production efficiency and economic benefits.

Belt grinding is one of the common grinding processes for titanium alloys, as shown in Figure 21. During the belt grinding process, three common abrasive effects—friction, plowing, and cutting—coexist in the grinding zone. When the belt wears severely, it becomes difficult to accurately describe the relevant grinding mechanisms and precisely control the workpiece quality. In response to this, Wan et al. [108] analyzed the abrasive wear mechanism of single diamond grains in flexible scribing of titanium alloys during belt grinding. Through a series of theoretical and experimental work on flexible scribing of titanium alloys with single-crystal diamond, the results indicated that grain size has a significant influence on the wear of diamond abrasive grains. Zhao et al. [109] experimentally investigated the grinding mechanism of individual diamond clusters in alloy flexible scratching. The results showed that force and temperature are the primary factors affecting the wear of diamond clusters, while the influence of friction speed is relatively minor compared to the former.

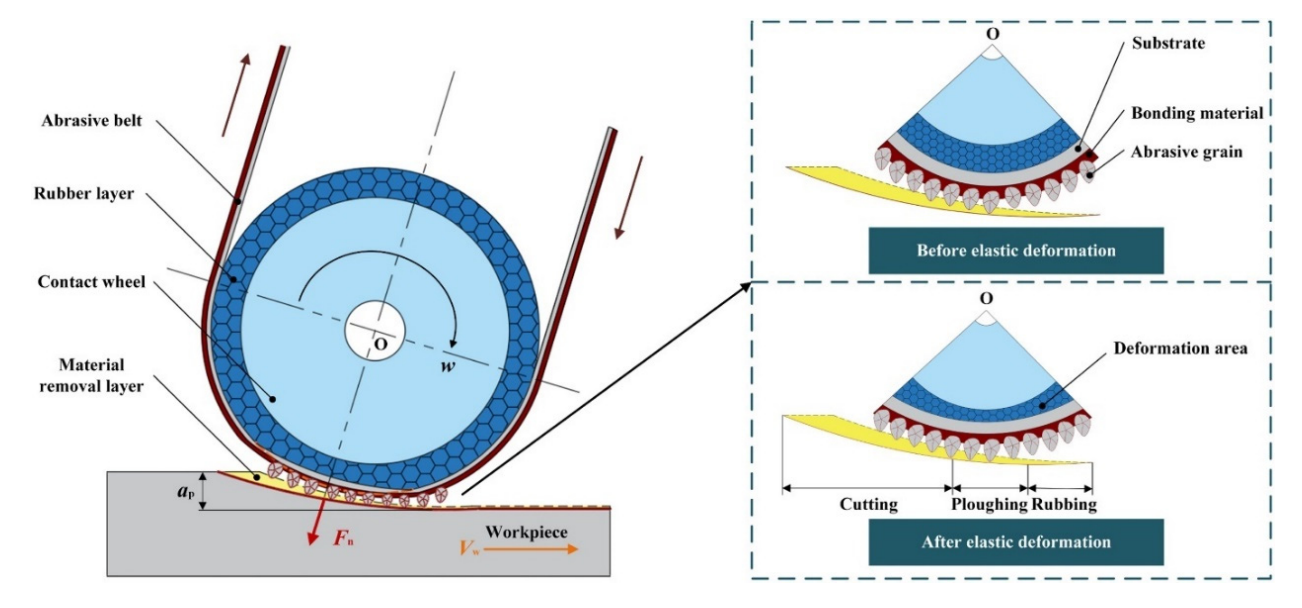


Figure 21. Principle of belt grinding.

Different processing methods can also have an impact on the material removal mode. Compared to conventional grinding (CG), ultrasonic vibration-assisted grinding (UVAG) significantly improves the material removal rate. Cao et al. [110] conducted a comparative study of CG and UVAG processing methods for Inconel 718 nickel-based superalloy. The results showed that UVAG significantly reduced the grinding force and surface roughness by approximately 11% and 10%, respectively, compared to CG processing, with fewer surface defects on the processed surface. When the vibration amplitude was 6 μ m, the surface roughness reached its minimum value. Nik et al. [111] used UVAG to process Ti-6Al-4V alloy and found that the normal and tangential forces were reduced by 13.5% and 14.2%, respectively, while

the surface roughness in the feed direction decreased by about 10%. Gao et al. [112] observed that the surface treated by UVAG exhibited many obvious and uniform intermittent protrusions with a certain periodicity, and the surface was dense.

4.2. Grinding Force Model

4.2.1. Titanium Alloy

During the grinding of titanium alloys, plastic deformation is prone to occur. Additionally, the titanium element is susceptible to chemical reactions with elements such as carbon and nitrogen in the tool material, as well as oxygen in the air, due to the grinding temperature. This can easily lead to adhesion phenomena. Adhesion exacerbates the wear of the grinding wheel and significantly reduces the quality of the workpiece. Due to the different shapes and random distribution of abrasive grains, it is challenging to establish an accurate grinding force model under adhesion conditions. In response to this, Ren et al. [113] took the adhesion phenomenon generated during the grinding of titanium alloys as the basis and analyzed the intrinsic relationship between the grinding force and the percentage of adhesion area. They established a mathematical model for the grinding force under adhesion conditions for titanium alloy grinding. This model is also applicable to other materials that exhibit adhesion phenomena. However, due to the randomness of the shape of abrasive grains and their distribution on the surface of the grinding wheel, as well as the difficulty in controlling the geometric angles of the cutting edges, and considering that the bonding agent will also have an impact, the grinding process is rather complicated. Therefore, it is difficult to establish a relatively accurate mathematical model for grinding.

Titanium alloys, due to their excellent biocompatibility, low density, corrosion resistance, and other properties, are widely used in orthopedic implants such as bone plates, bone screws, artificial joints, *etc.* Due to the small size of these implants, traditional grinding wheels cannot guarantee the required machining accuracy, so CBN grinding heads are typically used for finishing. Zhu et al. [114] found that there is currently limited research on predictive models for cutting forces in CBN grinding heads and analysis of chatter stability in the machining of titanium alloy thin-walled components both domestically and internationally. Furthermore, most current grinding force models are applicable to traditional grinding wheel grinding. Therefore, they established a side grinding force model for CBN grinding heads based on single abrasive grains for the machining of TC4 titanium alloy thin-walled parts (As shown in Figure 22).

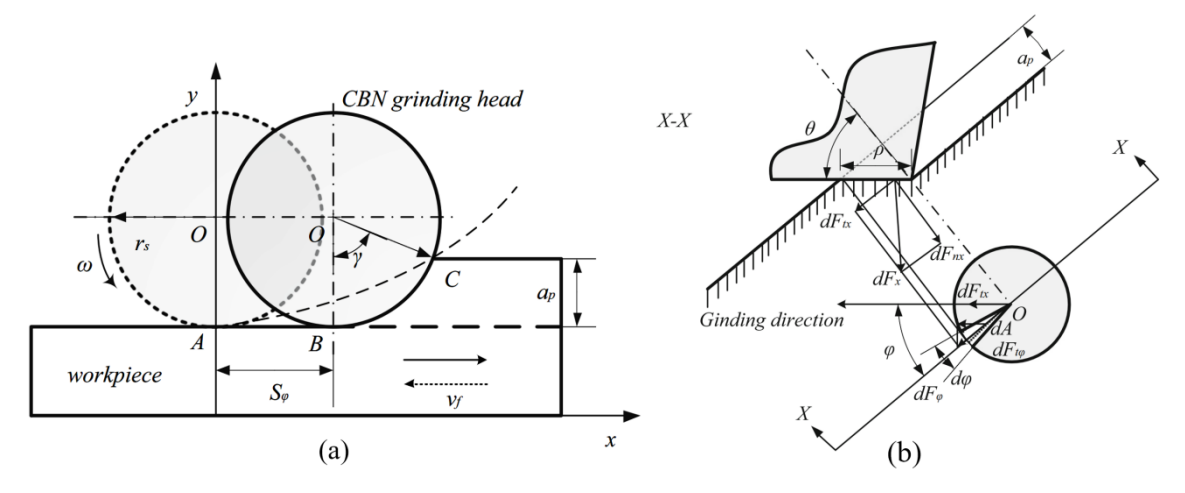


Figure 22. Side wear motion analysis: (a) schematic diagram of side grinding; (b) Schematic diagram of force model of a single grain in side grinding.

$$\begin{cases}
F_t = A_s c^{\beta - 2\alpha} b a_p^{1 - \frac{\alpha}{2}} \left(\frac{v_w}{v_s} \right)^{1 - \alpha} d_{\frac{\alpha}{se^{\frac{\alpha}{2}}}} \\
F_n = \frac{4}{\pi} A_s c^{\beta - 2\alpha} b \tan \theta a_p^{1 - \frac{\alpha}{2}} \left(\frac{v_w}{v_s} \right)^{1 - \alpha} d_{\frac{\alpha}{se^{\frac{\alpha}{2}}}}
\end{cases} \tag{29}$$

where, b is grinding head width, c is the coefficient related to the distribution density and shape of abrasive grains, d_{se} is the equivalent diameter of the grinding head, θ is the semi-angle of the a single grain, A_s is the proportional coefficient related to the number of static grinding blades.

When the processing area of titanium alloy is large, disc grinding is an effective grinding method to improve the

surface quality and machining accuracy of the workpiece. Based on the theory of flexible abrasive disc grinding, Duan et al. [115] considered the contact state between abrasive grains and the workpiece, and conducted experiments with different variables to establish a theoretical model for the normal grinding force in titanium alloy disc grinding from both macroscopic and microscopic perspectives. This model reveals the relationship between the grinding force and grinding parameters. From a macroscopic perspective, as shown in Figure 23a,b, the workpiece is assumed to be a rigid body, and the deformation force of the disc abrasive tool during elastic deformation when it contacts the workpiece surface is considered as the normal contact force. From a microscopic perspective, as shown in Figure 23c, the grinding force of a single abrasive grain is considered as the sum of the cutting deformation force and the friction force.

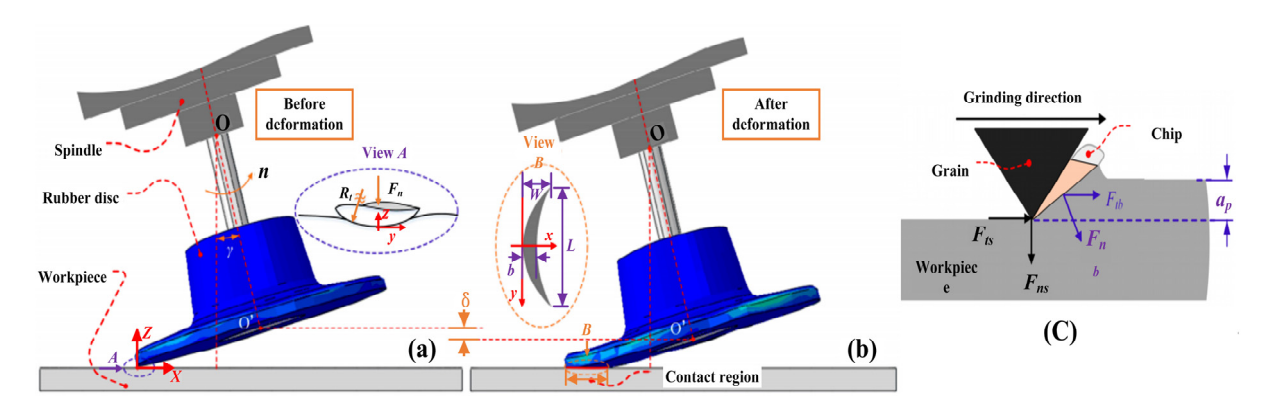


Figure 23. Grinding wheel disc grinding analysis: Contact status between the abrasive tool and the workpiece, (a) before deformation and (b) after deformation; (c) Modeling of a single abrasive grain in the grinding process.

Macroscopic Grinding Force:

$$F_{\rm n} = \frac{4}{3} \cdot E^* \cdot R_{\rm t}^{\frac{1}{2}} \cdot \delta^{\frac{3}{2}} \tag{30}$$

Microscopic Grinding Force:

$$F_{\rm n} = A_{\rm l} (\ln r_{\rm s} - \ln r_{\rm 0}) + \frac{2A_{\rm 2}}{3(1-\alpha)} \left(r_{\rm s}^{\frac{3(1-\alpha)}{2}} - r_{\rm 0}^{\frac{3(1-\alpha)}{2}} \right)$$
(31)

In the field of ultrasonic-assisted grinding, Liu et al. [116] observed that current research on ultrasonic-assisted grinding of titanium alloys mostly focuses on one-dimensional ultrasonic assistance, and there is relatively little research on the grinding mechanisms. Therefore, they conducted longitudinal-torsional ultrasonic-assisted grinding (LTUAG) processing with TC4 titanium alloy as the research object and established an LTUAG force model (as shown in Figure 24). This model aims to explore the wear patterns of grinding wheels during LTUAG of TC4 titanium alloy and improve the grinding efficiency and wheel life. The grinding force in this model is composed of two parts: the tangential and radial deformation resistances acting on the front surface of the abrasive grains and the tangential and radial friction forces between the bottom surface of the abrasive grains and the workpiece surface.

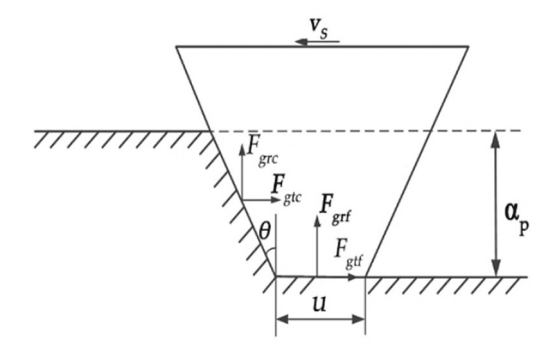


Figure 24. LTUAG Single grain grinding force diagram.

$$\begin{cases}
F_{n} = \frac{F_{0}a_{p}^{2r}tan^{r}\theta \cdot \left(u + a_{p}tan\theta\right)a_{p} \int_{0}^{t} \sqrt{v_{w}^{2} + v_{a}^{2} + 2v_{w}v_{a}cos(\omega t)dt}} \\
\int_{0}^{t} \sqrt{v_{w}^{2} + v_{s}^{2} + 2v_{w}v_{s}cos\left[\omega t + \frac{b}{R}sin(2\pi ft + \varphi)\right] + \left(2\pi fa\right)^{2}cos^{2}(2\pi ft)dt} \\
+ k_{1}a_{p}^{a_{1}}k_{2}a_{p}^{a_{2}}
\end{cases}$$

$$F_{\tau} = \frac{\pi F_{0}a_{p}^{2r}tan^{r-1}\theta \cdot \left(u + a_{p}tan\theta\right)a_{p} \int_{0}^{t} \sqrt{v_{w}^{2} + v_{a}^{2} + 2v_{w}v_{a}cos(\omega t)dt}} \\
+ \int_{0}^{t} \sqrt{v_{w}^{2} + v_{s}^{2} + 2v_{w}v_{s}cos\left[\omega t + \frac{b}{R}sin(2\pi ft + \varphi)\right] + (2\pi fa)^{2}cos^{2}(2\pi ft)dt}} \\
+ \mu k_{1}a_{p}^{a_{1}}k_{2}a_{p}^{a_{2}}
\end{cases}$$
(32)

where, b is the torsional ultrasonic vibration amplitude, A is the longitudinal ultrasonic vibration amplitude, f_b is the torsional-ultrasonic vibration frequency, f_a is the longitudinal ultrasonic vibration frequency, φ is the phase difference between longitudinal and torsional vibration.

4.2.2. Magnesium Alloy

Magnesium alloys are highly favored in the field of biomedical implant materials due to their elastic modulus similar to human bone and excellent biocompatibility. However, their insufficient wear resistance and corrosion resistance in the human environment, along with excessively fast degradation rates, may result in the implant losing its effectiveness before the bone has fully healed. Therefore, reducing the surface roughness of magnesium alloys and enhancing their surface integrity to improve their wear and corrosion resistance is crucial. Additionally, polishing the surface of magnesium implants not only optimizes their surface quality but also provides favorable conditions for subsequent thin-film plating and drug-coating processes. Due to the flammability and brittleness of magnesium alloys, traditional processing methods are difficult to use for their surface polishing. In response, Li et al. [117] proposed a composite magnetic pole device for surface grinding treatment of AZ31B magnesium alloy and established a grinding force prediction model (as shown in Figure 25).

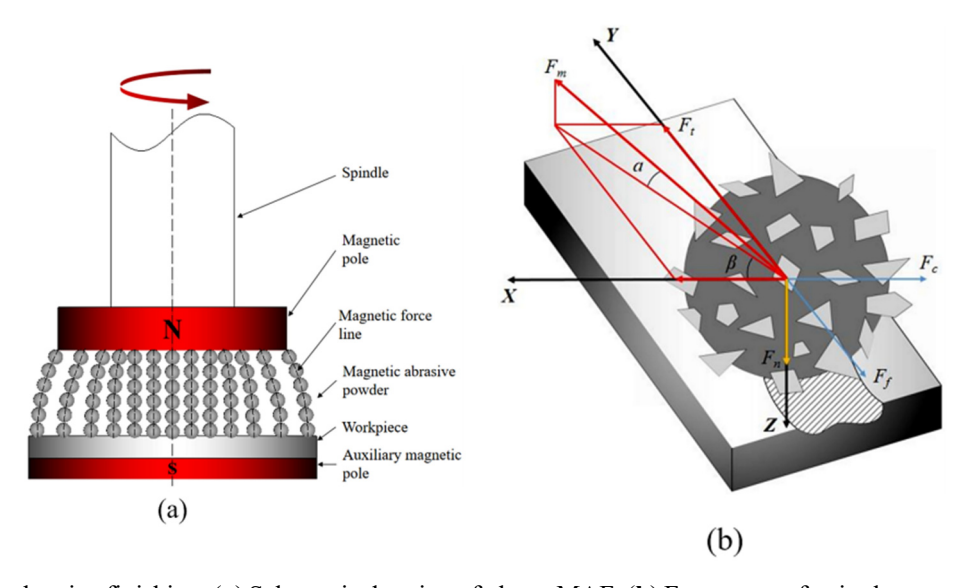


Figure 25. Magnetic abrasive finishing: (a) Schematic drawing of planar MAF; (b) Force state of a single magnetic abrasive powder.

The normal force of MAP F_n :

$$F_n = \frac{B^2}{16\mu_0} \cdot \frac{3\pi^2 d_m^2 V_m(\mu_i - 1)}{3V_m(2 + \mu_i) + \pi V_i(\mu_i - 1)}$$
(33)

Table 4 lists the relevant parameters and model errors of the bio-alloy grinding force model.

| Workpiece Material | References | Model Categories | Error |
|-----------------------|------------|--|--------|
| | [113] | Based on material adhesion phenomenon | 14.40% |
| Ti4i | [114] | based on the actual geometry and abrasive characteristics of CBN grinding hea | |
| Titanium alloy | [115] | Based on macro and micro theory | 6.975% |
| | [116] | Based on single grain grinding force | / |
| Magnesium alloy | [117] | The magnetic field force generated by the magnetic poles on the abrasive particles | / |

Table 4. Bio-alloy grinding force model.

4.3. Application of Models

Titanium Alloy

Feng et al. [118] conducted simulation analysis on their constructed grinding force model for diamond wheel grinding of titanium alloys, and based on the simulation results, performed experimental analysis to explore the influence of changes in processing parameters on the grinding force of the grinding wheel. Theoretical analysis of the force state of the grinding wheel was also carried out, based on both theoretical and experimental results, it was found that as the grinding wheel speed increases, the grinding force gradually decreases, while an increase in feed rate and grinding depth leads to an increase in the grinding force. When the processing parameters change, the change trends of both the theoretical and experimental values tend to be consistent, with the average theoretical and experimental error within 5%.

Liu et al. [119] conducted belt grinding experiments to investigate the changing characteristics of grinding force during the belt grinding process of titanium alloys. The experimental results, as shown in Figure 26, indicate that when the belt speed decreases, the feed rate of the workpiece increases, leading to a gradual increase in the belt grinding force. It was also observed that as the grinding force increases, the number of surface scratches on the workpiece increases, increasing surface roughness.

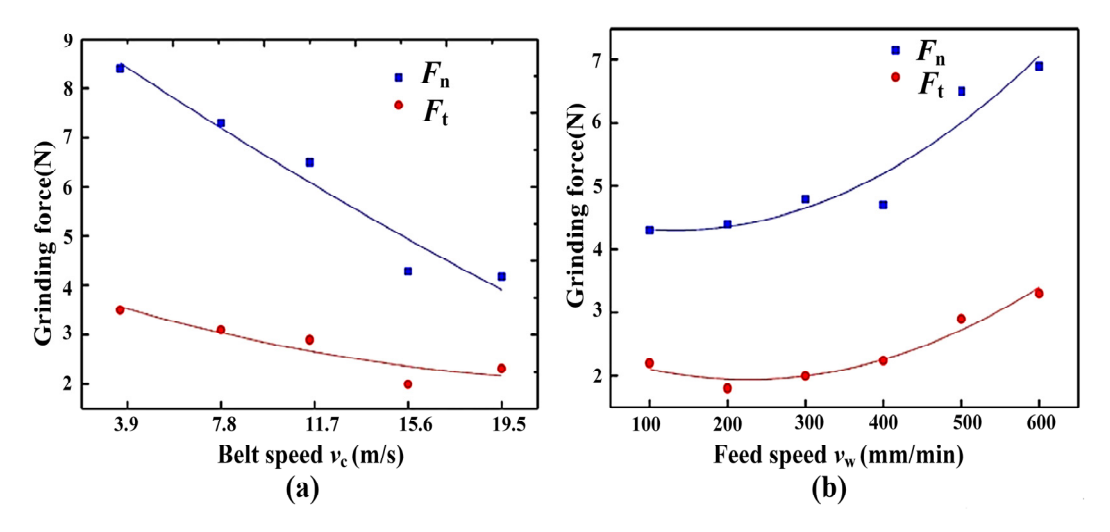


Figure 26. The influence of processing parameters on the belt grinding force: (a) Belt speed, (b) Feed speed.

Zhang et al. [120] conducted experimental validation on their established milling and grinding force model for titanium alloy spherical grinding heads and analyzed the influence of processing parameters on the grinding force. The experimental results indicate that the grinding force gradually decreases as the spindle speed increases. Specifically, when the spindle speed increases from 1000 r/min to 4000 r/min, the grinding force decreases by 60%. Additionally, as the feed rate and grinding depth increases, the grinding force also increases. When the feed rate increases from 40 mm/min to 160 mm/min, the milling and grinding force doubles. Similarly, when the milling and grinding depth increases from 0.02 mm to 0.05 mm, the milling and grinding force increases from 0.85 N to 2.49 N.

Wang et al. [121] conducted experimental validation on a single abrasive grain grinding force model established based on the relationship between the deformation force of abrasive chips and the cross-sectional area of abrasive grains, as well as the relationship between normal pressure and indentation depth. They also established a connection between the grinding force of a single abrasive grain and the grinding force per unit width. The experimental results show that the grinding force increases approximately linearly with the grinding depth of the grinding wheel. Reducing the grinding

depth of the grinding wheel and the feed rate of the workpiece can effectively decrease the grinding force per unit width.

Huang et al. [122] simplified the contact model between the contact wheel and the workpiece based on Hertzian contact theory, analyzed the principle of ultrasonic vibration belt grinding, and studied the motion characteristics of abrasive grains with ultrasonic assistance. By dividing the grinding force into two components: the cutting deformation force and the friction force, they analyzed the influence of ultrasonic vibration on both. Experimental results indicate that the introduction of ultrasonic vibration can effectively reduce the grinding force. This is because ultrasonic vibration can effectively increase the grinding speed of abrasive grains, change the grinding direction, and simultaneously reduce the uncut deformation thickness and the friction coefficient, thereby decreasing the friction force generated during cutting. Under the coupling of these effects, ultrasonic vibration can effectively reduce the grinding force. Qin et al. [123] also studied ultrasonic-assisted grinding of titanium alloys and proposed a physics-based prediction model for the grinding force in ultrasonic-assisted grinding of titanium alloys. This model was validated and analyzed through grinding experiments. As shown in Figure 27, the grinding force gradually decreases as the spindle speed increases. Conversely, an increase in feed rate leads to an increase in the grinding force.

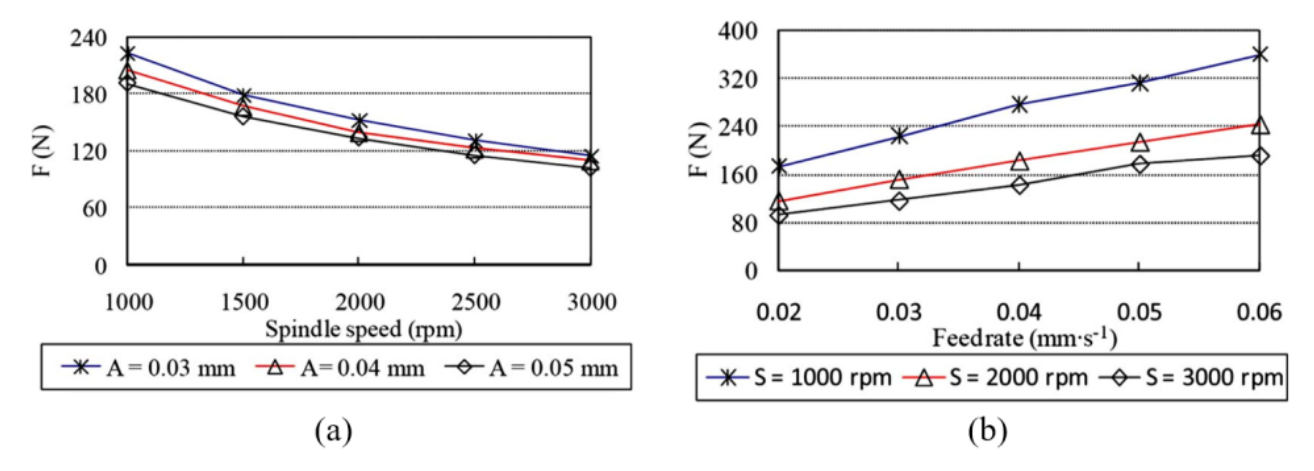


Figure 27. The influence of spindle speed and feed speed on grinding force: (a) Spindle speed, (b) Feed rate.

Lan et al. [124] combined the mechanochemical effect with ultrasonic vibration in the grinding process of titanium alloys and conducted ultrasonic grinding experiments on the surface and side of titanium alloys. As shown in the experimental results depicted in Figure 28, the mechanochemical effect can further reduce the grinding force during ultrasonic-assisted grinding. With the increase in ultrasonic amplitude, the reduction in grinding force gradually increases, indicating a significant synergistic effect between the two.

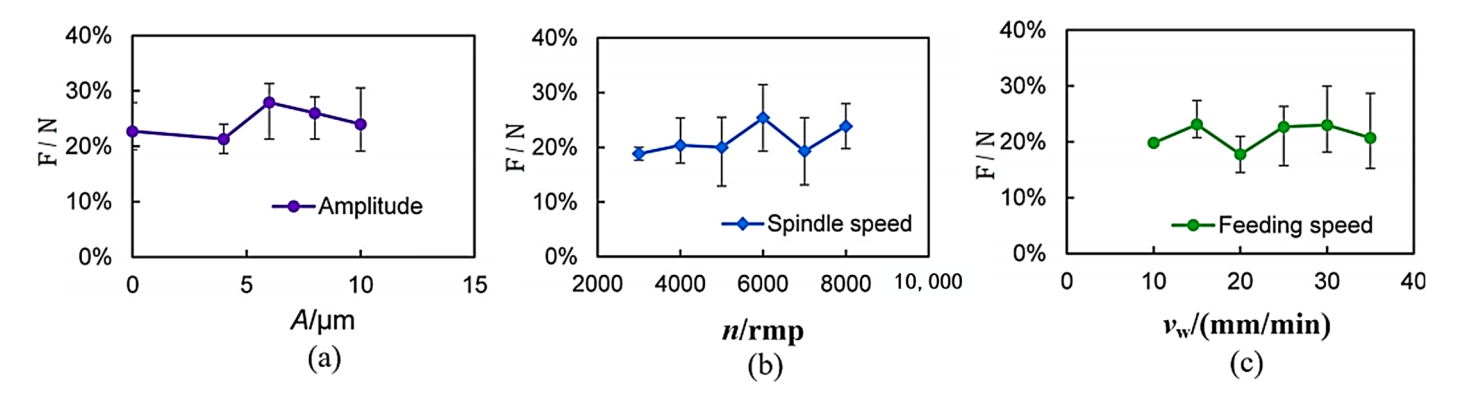


Figure 28. Effects of different processing parameters on ultrasonic assisted grinding force: (a) Aumplitude, (b) Spindle speed, (c) Feeding speed.

The relevant grinding parameters and effects in the application of the bio-alloy grinding force model are shown in Table 5.

| Workniege | | | Pro | cessing | Parame | | | | |
|-----------------------|------------|-----------|--------------------------|---------------------------|------------|-----------------|-----------|--------------------------|---|
| Workpiece Material | References | Vs m/s | V _W mm/min | <i>a</i> _p /mm | n r/min | <i>Α</i> /μm | f ∕kHz | Tool | Influence |
| | [118] | 960 | 50 | 0.03 | / | / | / | Diamond grinding wheel | Grinding forces F_n and F_t decrease with the increase of v_s , while |
| | | 1440 | 440 70 0.03 | 0.03 | | | | | |
| | | 1440 | 50 | 0.01 | | | | | |
| Titanium alloy | [120] | / | 40 | 0.02 | 4000 | / | / | Spherical polishing tool | |
| | [121] | 24 | 0.30 m/s | 0.3 | / | / | / | Borazon grinding wheel | they increase with greater values a_p and |
| | [123] | / | / | / | 300 | 30 | 20 | Diamond grinding wheel | $v_{ m w}$ |
| | [124] | / | 20 | 20 | 4000 | 0-10 | | PCD tool | _ |

Table 5. The relationship between grinding force and machining parameters of biological alloy.

5. Conclusions and Prospects

5.1. Conclusions

This paper comprehensively summarizes the prediction models of grinding force during the grinding process of bone tissue and alternative materials. Based on different material removal mechanisms, the grinding force prediction models for bone, bioinert ceramics, and bioalloys are established. The influence and mapping relationship between different processing parameters (such as feed rate and cutting depth) and grinding force are explored overall. It provides theoretical guidance and support for improving the grinding quality of bone tissue and its substitute materials. The main conclusions are as follows:

- (1) Due to the heterogeneity and anisotropy of bone tissue material, its complexity during actual processing is more pronounced compared to metallic materials. Currently, research on grinding force models mainly focuses on mechanical models and numerical models, which are validated by experimental data for accuracy. These models have shown unique advantages in parameter optimization and improving processing quality. For example, the model developed by Sun [60] takes into account the geometric features of abrasive particles, ultrasonic vibration parameters, and dynamic changes in the contact arc length. Experimental validation shows that the average errors in the x, y, and z axes are 10.37%, 6.85%, and 7.81%, respectively, effectively proving its applicability.
- (2) Bioinert ceramics are hard and brittle materials with high brittleness and hardness, and grinding is often used in their machining. In grinding force prediction models, factors such as plastic removal, brittle fracture, ductile-to-brittle transition, crack formation, and maximum undeformed chip thickness are typically considered. The error range for grinding force models is between 3.5% and 22.78%. Model validation has shown that, in conventional grinding, cutting force decreases as wheel speed increases, while grinding force increases with higher feed rates and cutting depths. In ultrasonic-assisted grinding, higher ultrasonic amplitude and frequency result in a reduction in cutting force. Compared to conventional grinding, the cutting force in ultrasonic-assisted grinding is reduced by approximately 30%.
- (3) Bioalloy materials primarily remove material through plastic deformation. In the study of grinding force prediction models, the effects of abrasive particle size, shape, wheel type, and processing parameters are often considered. The changes in related elements within the alloy material also need to be taken into account, such as the tendency for titanium alloys to chemically react with carbon, nitrogen, and other elements in the tool material, leading to adhesion phenomena. The error range of bioalloy grinding force models is between 6.975% and 16%.

5.2. Prospects

(1) Current grinding force models for biological bone tissue are primarily based on the assumptions of homogeneity and isotropy, and are researched based on the cutting theory of metallic materials in the field of machining. However, these models deviate from the true mechanical properties of bone materials and the actual experimental results, limiting the accuracy and practical applicability of the theoretical models. Therefore, it is necessary to develop a heat transfer and cutting force theoretical model tailored to the non-homogeneous and anisotropic processing characteristics of bone tissue. Additionally, existing models often consider only a limited set of factors. Future models could incorporate multiple factors (including heat generation, cutting force, tool deformation, changes in friction conditions, *etc.*) to construct a more comprehensive, multi-factor grinding force prediction model.

- (2) Current research on grinding force prediction models for bioinert ceramics mainly focuses on applying general removal mechanisms for hard and brittle materials rather than conducting detailed studies on the removal mechanisms specific to different types of ceramics. Furthermore, these models do not fully account for the material property differences between bioinert ceramics and other hard and brittle materials (such as glass), as well as between different types of ceramics. As a result, the accuracy of existing grinding force models is somewhat limited, and further in-depth exploration and research are urgently needed.
- (3) Although traditional alloy materials exhibit good stability and durability in the human body, their long-term implantation may lead to adverse effects such as infections and rejection reactions. Additionally, their non-biodegradable nature poses extra challenges in medical waste disposal. Therefore, the development of biodegradable medical materials is particularly important. Furthermore, given the high hardness and strength of alloy materials such as titanium alloys, using conventional cutting tools results in significant tool wear, relatively short tool life, high surface roughness, and insufficient precision in the machined parts. As a result, exploring and developing new cutting tool materials and technologies will be one of the key directions for future research.

Author Contributions

Conceptualization, X.K. and M.Y.; Methodology, X.K.; Software, Z.L.; Validation, M.Y., C.L. (Chuankun Li), X.C. and Y.Z.; Investigation, X.K.; Data Curation, C.L. (Changhe Li); Writing—Original Draft Preparation, X.K.; Writing—Review & Editing, M.Y.; Supervision, M.L., X.M. and B.L.; Funding Acquisition, M.Y.

Ethics Statement

Not applicable.

Informed Consent Statement

Not applicable.

Data Availability Statement

The data that support the findings of this study are available from the corresponding author, upon reasonable request.

Funding

This study was financially supported by the National Natural Science Foundation of China (Grant Nos. 52205481, 52305477), Support plan for Outstanding Youth Innovation Team in Universities of Shandong Province (2023KJ114), Young Talent of Lifting engineering for Science and Technology in Shandong, China (SDAST2024QTA043), Key Lab of Industrial Fluid Energy Conservation and Pollution Control (Ministry of Education) (CK-2024-0033), General Program of Shandong Provincial Natural Science Foundation (ZR2024ME205).

Declaration of Competing Interest

The authors declare that they have no known competing financial interests or personal relationships that could have appeared to influence the work reported in this paper.

References

- Zheng QC, Zhu YY, Fan ZH, Wang DH, Zhang CQ, Liu SH, et al. Multi-objective optimization of cortical bone grinding parameters based on particle swarm optimization. *Proc. Inst. Mech. Eng. Part H-J. Eng. Med.* 2023, 237, 1400–1408. doi:10.1177/09544119231206455.
- 2. Theler JM. Bone tissue substitutes and replacements. *Curr. Opin. Otolaryngol. Head Neck Surg.* **2011**, *19*, 317–321. doi:10.1097/MOO.0b013e32834883f2.
- 3. Bock RM, Mcentire BJ, Bal BS, Rahaman MN, Boffelli M, Pezzotti G. Surface modulation of silicon nitride ceramics for orthopaedic applications. *Acta Biomater.* **2015**, *26*, 318–330. doi:10.1016/j.actbio.2015.08.014.
- 4. Cai BY, Yuan DL, Li GD, Lei K, Han M, Huang YZ, et al. Promoting Osseointegration of New Innocuous Ti-18Zr-13Mo Implant Through Constructing Hierarchically Structured Bioactive Coating. *Met. Mater. Int.* **2023**, *29*, 3402–3417. doi:10.1007/s12540-023-01455-1.

- 5. Huang R, Lu SM, Han Y. Role of grain size in the regulation of osteoblast response to Ti-25Nb-3Mo-3Zr-2Sn alloy. *Colloids Surf. B-Biointerfaces* **2013**, *111*, 232–241. doi:10.1016/j.colsurfb.2013.06.007.
- 6. Wathanyu K, Tuchinda K, Daopiset S, Sirivisoot S. Corrosion resistance and biocompatibility of cold-sprayed titanium on 316L stainless steel. *Surf. Coat. Technol.* **2022**, *445*, 128721. doi:10.1016/j.surfcoat.2022.128721.
- 7. Rodrigues AC, De Souza RNF, Galisa OF, França TV, Bianchi EC, Foschini CR. Effect of Grinding Parameters on Surface Finishing of Advanced Ceramics. *Mater. -Rio De Jan.* **2016**, *21*, 1012–1020. doi:10.1590/s1517-707620160004.0093.
- 8. Gao LM, Lu XJ, Zhang XG, Meng QG, Jin ZM. Lubrication Modelling of Artificial Joint Replacements: Current Status and Future Challenges. *Lubricants* **2022**, *10*, 238. doi:10.3390/lubricants10100238.
- 9. Feng JB, Chen R, Li B, Jiang BH, Li B. The Current Trend of Antibacterial Prostheses and Prosthetic Surface Coating Technologies to Prevent Prosthetic Joint Infection for Artificial Joint Replacement. *J. Biomater. Tissue Eng.* **2023**, *13*, 1046–1060. doi:10.1166/jbt.2023.3342.
- 10. Kuncická L, Kocich R, Lowe TC. Advances in metals and alloys for joint replacement. *Prog. Mater. Sci.* **2017**, *88*, 232–280. doi:10.1016/j.pmatsci.2017.04.002.
- 11. Ostrowski N, Lee B, Enick N, Carlson B, Kunjukunju S, Roy A, et al. Corrosion protection and improved cytocompatibility of biodegradable polymeric layer-by-layer coatings on AZ31 magnesium alloys. *Acta Biomater.* **2013**, *9*, 8704–8713. doi:10.1016/j.actbio.2013.05.010.
- 12. Han JJ, Wan P, Ge Y, Fan XM, Tan LL, Li JJ, et al. Tailoring the degradation and biological response of a magnesium-strontium alloy for potential bone substitute application. *Mater. Sci. Eng. C-Mater. Biol. Appl.* **2016**, *58*, 799–811. doi:10.1016/j.msec.2015.09.057.
- 13. Liu C, Tong SK, Yue YF, Wang HX, Song JP, Li YB, et al. Laser-based fabrication of superwetting titanium alloy with enhanced corrosion and erosion-corrosion resistance. *Colloids Surf. a-Physicochem. Eng. Asp.* **2024**, *688*, 133648. doi:10.1016/j.colsurfa.2024.133648.
- 14. Xu W, Lu X, Wang LN, Shi ZM, Lv SM, Qian M, et al. Mechanical properties, in vitro corrosion resistance and biocompatibility of metal injection molded Ti-12Mo alloy for dental applications. *J. Mech. Behav. Biomed. Mater.* **2018**, *88*, 534–547. doi:10.1016/j.jmbbm.2018.08.038.
- 15. Saji VS, Choe HC, Ko YM, Ahn H. Nanotube Morphology and Corrosion Resistance of a Low Rigidity Quaternary Titanium Alloy for Biomedical Applications. *J. Nanosci. Nanotechnol.* **2010**, *10*, 4635–4639. doi:10.1166/jnn.2010.1715.
- 16. Zhi PX, Liu LX, Chang JK, Liu CZ, Zhang QL, Zhou J, et al. Advances in the Study of Magnesium Alloys and Their Use in Bone Implant Material. *Metals* **2022**, *12*, 1500. doi:10.3390/met12091500.
- 17. Yang M, Ma H, Li ZH, Hao JC, Liu MZ, Cui X, et al. Force model in electrostatic atomization minimum quantity lubrication milling GH4169 and performance evaluation. *Front. Mech. Eng.* **2024**, *19*, 28. doi:10.1007/s11465-024-0800-8.
- 18. Wang WH, Wang F, Zhao HF, Yan K, Huang CL, Yin Y, et al. Injectable Magnesium-Zinc Alloy Containing Hydrogel Complex for Bone Regeneration. *Front. Bioeng. Biotechnol.* **2020**, *8*, 617585. doi:10.3389/fbioe.2020.617585.
- 19. Mohammadi H, Beddu S, Petra M, Sepantafar M, Ebadi M, Yap BK, et al. Advances in silicon nitride ceramic biomaterials for dental applications—A review. *J. Mater. Res. Technol. -JmrT* **2024**, *28*, 2778–2791. doi:10.1016/j.jmrt.2023.12.186.
- 20. Tang ZR, Li XF, Tan YF, Fan HS, Zhang XD. The material and biological characteristics of osteoinductive calcium phosphate ceramics. *Regen. Biomater.* **2018**, *5*, 43–59. doi:10.1093/rb/rbx024.
- 21. Wang JL, Zhang LL, Wang K. Bioactive ceramic-based materials: beneficial properties and potential applications in dental repair and regeneration. *Regen. Med.* **2024**, *19*, 257–278. doi:10.1080/17460751.2024.2343555.
- 22. Lemos CAA, Verri FR, Gomes JMD, Batista VED, Cruz RS, Oliveira H, et al. Ceramic versus metal-ceramic implant-supported prostheses: A systematic review and meta-analysis. *J. Prosthet. Dent.* **2019**, *121*, 879–886. doi:10.1016/j.prosdent.2018.09.016.
- 23. Chanda A, Singharoy R, Xue WC, Bose S, Bandyopadhyay A. Bone cell-materials interaction on alumina ceramics with different grain sizes. *Mater. Sci. Eng. C-Biomim. Supramol. Syst.* **2009**, *29*, 1201–1206. doi:10.1016/j.msec.2008.09.023.
- 24. Gao T, Xu PM, Wang W, Zhang YB, Xu WH, Wang YQ, et al. Force model of ultrasonic empowered minimum quantity lubrication grinding CFRP. *Int. J. Mech. Sci.* **2024**, *280*, 109522. doi:10.1016/j.ijmecsci.2024.109522.
- 25. Tanner KE. Bioactive ceramic-reinforced composites for bone augmentation. *J. R. Soc. Interface* **2010**, 7, S541–S557. doi:10.1098/rsif.2010.0229.focus.
- 26. Yang M, Kong M, Li CH, Long YZ, Zhang YB, Sharma S, et al. Temperature field model in surface grinding: A comparative assessment. *Int. J. Extrem. Manuf.* **2023**, *5*, 042011. doi:10.1088/2631-7990/acf4d4.
- 27. Yang YY, Yang M, Li CH, Li RZ, Said Z, Ali HM, et al. Machinability of ultrasonic vibration-assisted micro-grinding in biological bone using nanolubricant. *Front. Mech. Eng.* **2023**, *18*, 1. doi:10.1007/s11465-022-0717-z.
- 28. Babbar A, Jain V, Gupta D, Agrawal D, Prakash C, Singh S, et al. Experimental analysis of wear and multi-shape burr loading during neurosurgical bone grinding. *J. Mater. Res. Technol. -JmrT* **2021**, *12*, 15–28. doi:10.1016/j.jmrt.2021.02.060.
- 29. Liu MZ, Li CH, Yang M, Gao T, Wang XM, Cui X, et al. Mechanism and enhanced grindability of cryogenic air combined with biolubricant grinding titanium alloy. *Tribol. Int.* **2023**, *187*, 108704. doi:10.1016/j.triboint.2023.108704.
- 30. An QL, Fu YC, Xu JH. A new technology on enhancing heat transfer during grinding of titanium alloy. Ind. Lubr. Tribol. 2010,

- 62, 168-173. doi:10.1108/00368791011034557.
- 31. Yang M, Hao JC, Wu WT, Li ZH, Ma YQ, Zhou ZM, et al. Critical cutting thickness model considering subsurface damage of zirconia grinding and friction—Wear performance evaluation applied in simulated oral environment. *Tribol. Int.* **2024**, *198*, 109881. doi:10.1016/j.triboint.2024.109881.
- 32. Zhao ML, Xue BX, Li BH, Zhu JM, Song WB, Nie LX. Modeling of grinding force in longitudinal ultrasonic vibration-assisted grinding alumina ceramics and experimental evaluation. *Int. J. Adv. Manuf. Technol.* **2024**, *131*, 2325–2339. doi:10.1007/s00170-023-11590-z.
- 33. Li C, Duan J, Zhang XH, Shi ZY, Yuchi GZ, Zhang SH, et al. Grinding performance integrated experimental evaluation on alumina ceramics with leaf-vein bionic grinding wheel. *Int. J. Adv. Manuf. Technol.* **2022**, *121*, 2525–2537. doi:10.1007/s00170-022-09502-8.
- 34. Zhang GF, Wang ZG, Chen WX, Li JT, Sun H, Zhang K. Single-Point Grinding of Alumina and Zirconia Ceramics Under Two-Dimensional Compressive Prestress. *Int. J. Precis. Eng. Manuf.* **2020**, *21*, 1–9. doi:10.1007/s12541-019-00232-8.
- 35. Zhang XH, Kang ZX, Li S, Shi ZY, Wen DD, Jiang J, et al. Grinding force modelling for ductile-brittle transition in laser macro-micro-structured grinding of zirconia ceramics. *Ceram. Int.* **2019**, *45*, 18487–18500. doi:10.1016/j.ceramint.2019.06.067.
- 36. Dambatta YS, Sarhan AAD, Sayuti MB, Bin Abd Shukor MH. Fuzzy logic method to investigate grinding of alumina ceramic using minimum quantity lubrication. *Int. J. Appl. Ceram. Technol.* **2019**, *16*, 1668–1683. doi:10.1111/ijac.13219.
- 37. Liu DW, Li CH, Xu PM, Wang W, Zhang YB, Yang M, et al. SiCp/Al composites from conventional to empowered machining: Mechanisms and processability. *Compos. Struct.* **2024**, *346*, 118433. doi:10.1016/j.compstruct.2024.118433.
- 38. Li CH, Zhang YB, Said Z. Enhanced manufacture technology based on emission reduction and carbon reduction in cutting and grinding. *Int. J. Adv. Manuf. Technol.* **2024**, *131*, 1963–1974. doi:10.1007/s00170-024-13216-4.
- 39. Li BK, Ding WF, Zhu YJ, Li CH, Zhang YB, Yang M, et al. Design and grindability assessment with cup shaped electroplated CBN wheel grinding turbine disc slots of powder metallurgy superalloy FGH96. *Chin. J. Aeronaut.* **2024**, *37*, 521–534. doi:10.1016/j.cja.2023.12.030.
- 40. Ji CH, Sheng R, Wu H, Zhou ZM, Yan X, Dong L, et al. Bibliometric analysis and research trends in minimum quantity lubrication for reducing cutting forces. *Int. J. Adv. Manuf. Technol.* **2024**, *135*, 4995–5033. doi:10.1007/s00170-024-14793-0.
- 41. Gu GQ, Wu SJ, Wang DZ, Zhang BX, Li CH, Liang ZQ. Machining mechanism of metal glass cutting based on ultrasonic vibration tool path. *Int. J. Adv. Manuf. Technol.* **2024**, *130*, 2343–2368. doi:10.1007/s00170-023-12818-8.
- 42. Gong P, Zhang YB, Wang CJ, Cui X, Li RZ, Sharma S, et al. Residual stress generation in grinding: Mechanism and modeling. *J. Mater. Process. Technol.* **2024**, *324*, 118262. doi:10.1016/j.jmatprotec.2023.118262.
- 43. Irazu E, Alonso U, Izquierdo B, Godino L. Grinding of C/SiC ceramic matrix composites: Influence of grinding parameters on tool wear. *Wear* **2024**, *558*, 205582. doi:10.1016/j.wear.2024.205582.
- 44. Liu MY, Wang J, Li Y, Cheng KY, Huan Y, Li N. Development of mechanical equivalent porous structures for 3D-printed artificial femoral heads. *Acta Mech. Sin.* **2025**, *41*, 624089. doi:10.1007/s10409-024-24089-x.
- 45. Ganjiani M, Ghobadi S, Faraji G. Evaluating the ductile failure characteristics of CuZn30 brass under different stress conditions. *Eng. Fail. Anal.* **2025**, *167*, 108932. doi:10.1016/j.engfailanal.2024.108932.
- 46. Zhang SY, Qu DJ, Luo BW, Wang LC, Li H, Wang HJ. Regulation of Osteogenic Differentiation of hBMSCs by the Overlay Angles of Bone Lamellae-like Matrices. *Acs Appl. Mater. Interfaces* **2024**, *16*, 56801–56814. doi:10.1021/acsami.4c12847.
- 47. Cojocaru E, Oprea M, Vlasceanu GM, Nicolae MC, Popescu RC, Mereuta PE, et al. Dual nanofiber and graphene reinforcement of 3D printed biomimetic supports for bone tissue repair. *Rsc Adv.* **2024**, *14*, 32517–32532. doi:10.1039/d4ra06167e.
- 48. Anetai Y, Doi K, Takegawa H, Koike Y, Yui M, Yoshida A, et al. Diffusion equation quantification: Selective enhancement algorithm for bone metastasis lesions in CT images. *Phys. Med. Biol.* **2024**, *69*, 245007. doi:10.1088/1361-6560/ad965c.
- 49. Liu F, Wang HY, Zhao B, Zhang W, Wang Q, Niu YS, et al. Study on deposition of biomedical Ta coating on Ti6Al4V alloy substrate by CVD and its properties. *Surf. Coat. Technol.* **2025**, *495*, 131593. doi:10.1016/j.surfcoat.2024.131593.
- 50. Kasman S, Ozan S, Wen CE. Influence of pulse duration and frequency of laser surface texturing on the surface roughness and microstructure of CoCr28Mo alloy for biomedical applications. *Mater. Test.* **2024**, *67*, 36–48. doi:10.1515/mt-2024-0139.
- 51. Kaneta H, Shoji T, Kato Y, Shozen H, Ueki S, Morita H, et al. Relationship Between the Subchondral Trabecular Bone Microstructure in the Hip Joint and Pain in Patients with Hip Osteoarthritis. *Cartilage* **2024**, *131*, 2254–4459. doi:10.1177/19476035241302978.
- 52. Guo W, Li P, Wei YT, Zhao L, Pang YH, Huang YJ, et al. Ionic substitution through bredigite doping for microstructure and performance adjustment in DLP 3D-printed TPMS porous HA bone scaffolds. *Virtual Phys. Prototyp.* **2024**, *19*, e2423840. doi:10.1080/17452759.2024.2423840.
- 53. Al-Goraee A, Al-Shami A, Alshami AS, Dhasarathy A, Ismail N, Guidinger J, et al. A hierarchically porous and SLIT3-releasing scaffold for bone tissue engineering applications. *J. Mater. Sci.* **2024**, *60*, 414–431. doi:10.1007/s10853-024-10379-z.
- 54. Wang ZH, Chen HW, Song QH, Reng YH, Sui JB, Shu LM. A Review on Cutting Mechanism for Bone Material. *J. Mech. Eng.* **2021**, *57*, 2–32.

- 55. Yang Y, Ling C, Li Y, Peng S, Xie D, Shen L, et al. Microstructure development and biodegradation behavior of additively manufactured Mg-Zn-Gd alloy with LPSO structure. *J. Mater. Sci. Technol.* **2023**, *144*, 1–14. doi:10.1016/j.jmst.2022.09.059.
- 56. Yang M, Li CH, Zhang YB, Wang YG, Li BK, Li RZ. Theoretical Analysis and Experimental Research on Temperature Field of Microscale Bone Grinding under Nanoparticle Jet Mist Cooling. *J. Mech. Eng.* **2018**, *54*, 194–203.
- 57. Zou L, Wen DH, Zhang LH, Chen ZZ, Xiao YT, Liang J. Computational Model and Experimental Study for Bone Tissue Grinding Forces. *China Mech. Eng.* **2020**, *31*, 3016–3023.
- 58. Danda A, Kuttolamadom MA, Tai BL. A mechanistic force model for simulating haptics of hand-held bone burring operations. *Med. Eng. Phys.* **2017**, *49*, 7–13. doi:10.1016/j.medengphy.2017.06.041.
- 59. Gaziano P, Monaldo E, Falcinelli C, Vairo G. Elasto-damage mechanics of osteons: A bottom-up multiscale approach. *J. Mech. Phys. Solids* **2022**, *167*, 104962. doi:10.1016/j.jmps.2022.104962.
- 60. Sun JG, Li CH, Zhou ZM, Liu B, Zhang YB, Yang M, et al. Material Removal Mechanism and Force Modeling in Ultrasonic Vibration-Assisted Micro-Grinding Biological Bone. *Chin. J. Mech. Eng.* **2023**, *36*, 129. doi:10.1186/s10033-023-00957-8.
- 61. Zhu YY, Zheng QC, Zhang SQ, Wang GL, Hu YH. Simulation and research on ultrasonic vibration-assisted grinding of cortical bone. *J. Tianjin Univ. Technol.* **2024**, *26*, 1–6.
- 62. Hu YH, Hu XC, Fan ZH, Liu Z, Zhang CQ, Fu WH. Cortical bone grinding mechanism modeling and experimental study for damage minimization in craniotomy. *Proc. Inst. Mech. Eng.* **2021**, *236*, 320–328. doi:10.1177/09544119211060135.
- 63. Zhu Z, Hu ZW, Zhang ZB, Xu XP. Study on grinding force of bovine cortical bone by different grinding wheels. *Diam. Abras. Eng.* **2014**, *34*, 13–16.
- 64. Liao ZR, Axinte DA. On chip formation mechanism in orthogonal cutting of bone. *Int. J. Mach. Tools Manuf.* **2016**, *102*, 41–45. doi:10.1016/j.ijmachtools.2015.12.004.
- 65. Liao ZR, Axinte DA, Gao T. On modelling of cutting force and temperature in bone milling. *J. Mater. Process. Technol.* **2019**, *266*, 627–638. doi:10.1016/j.jmatprotec.2018.11.039.
- 66. Choudhary A, Paul S. Surface generation in high-speed grinding of brittle and tough ceramics. *Ceram. Int.* **2021**, *47*, 30546–30562. doi:10.1016/j.ceramint.2021.07.233.
- 67. Choudhary A, Chakladar ND, Paul S. Identification and estimation of defects in high-speed ground C/SiC ceramic matrix composites. *Compos. Struct.* **2021**, *261*, 24–29. doi:10.1016/j.compstruct.2020.113274.
- 68. Kuzin VV, Grigoriev SN, Volosova MA. Computer Engineering of the Surface Layer of Ground Al₂O₃-TiC Ceramics. Thermal Analysis. *Refract. Ind. Ceram.* **2020**, *61*, 418–423. doi:10.1007/s11148-020-00496-y.
- 69. Chen SG, Lin B, Han XS, Liang XH. Automated inspection of engineering ceramic grinding surface damage based on image recognition. *Int. J. Adv. Manuf. Technol.* **2013**, *66*, 431–443. doi:10.1007/s00170-012-4338-2.
- 70. Zhao DL, Yu KD, Sun TF, Jing XR, Wan YZ, Chen KF, et al. Material-Structure-Function Integrated Additive Manufacturing of Degradable Metallic Bone Implants for Load-Bearing Applications. *Adv. Funct. Mater.* **2023**, *33*, 76–80. doi:10.1002/adfm.202213128.
- 71. Xu ZR. Research trends and progress in the field of metal materials and bone repair: Comprehensive bibliometric and visual analysis (2012–2021). *Front. Mater.* **2022**, *9*, 135–142. doi:10.3389/fmats.2022.954525.
- 72. Lv YT, Wang BH, Liu GH, Tang YJ, Lu EY, Xie KG, et al. Metal Material, Properties and Design Methods of Porous Biomedical Scaffolds for Additive Manufacturing: A Review. *Front. Bioeng. Biotechnol.* **2021**, *9*, 267–274. doi:10.3389/fbioe.2021.641130.
- 73. Liang WQ, Dong YQ, Shen HL, Shao RY, Wu XD, Huang XG, et al. Materials science and design principles of therapeutic materials in orthopedic and bone tissue engineering. *Polym. Adv. Technol.* **2021**, *32*, 4573–4586. doi:10.1002/pat.5445.
- 74. Liu Y, Lv SC, Sun XW, Yang HR, Dong ZX, Mu SB, et al. Comparative study of tool wear mechanisms in drilling ZrO₂ ceramics using various tool types. *J. Braz. Soc. Mech. Sci. Eng.* **2024**, *46*, 635. doi:10.1007/s40430-024-05220-2.
- 75. Li QZ, Wu Z, Ji BF, Zhang S, Tu R. Cutting Performance of TiN/TiSiN Coated Tool during Turning of Ti6Al4V Titanium Alloy. *J. Mater. Eng. Perform.* **2024**, *78*, 886–894. doi:10.1007/s11665-024-09815-7.
- 76. Ming WY, Jia HJ, Zhang HM, Zhang Z, Liu K, Du JG, et al. A comprehensive review of electric discharge machining of advanced ceramics. *Ceram. Int.* **2020**, *46*, 21813–21838. doi:10.1016/j.ceramint.2020.05.207.
- 77. Bifano TG, Dow TA, Scattergood RO. Ductile-Regime Grinding: A New Technology for Machining Brittle Materials. *J. Eng. Ind.* **1991**, *113*, 184–189. doi:10.1115/1.2899676.
- 78. Yang M, Li CH, Zhang YB, Jia DZ, Li RZ, Hou YL, et al. Effect of friction coefficient on chip thickness models in ductile-regime grinding of zirconia ceramics. *Int. J. Adv. Manuf. Technol.* **2019**, *102*, 2617–2632. doi:10.1007/s00170-019-03367-0.
- 79. Sun YL, Zuo DW, Wang HY, Zhu YW, Li J. Mechanism of brittle-ductile transition of a glass-ceramic rigid substrate. *Int. J. Miner. Metall. Mater.* **2011**, *18*, 229–233. doi:10.1007/s12613-201-0427-0.
- 80. Li ZP, Zhang FH, Luo XC, Chang WL, Cai YK, Zhong WB, et al. Material removal mechanism of laser-assisted grinding of RB-SiC ceramics and process optimization. *J. Eur. Ceram. Soc.* **2019**, *39*, 705–717. doi:10.1016/j.jeurceramsoc.2018.11.002.
- 81. Baraheni M, Amini S. Predicting subsurface damage in silicon nitride ceramics subjected to rotary ultrasonic assisted face grinding. *Ceram. Int.* **2019**, *45*, 10086–10096. doi:10.1016/j.ceramint.2019.02.055.
- 82. Li C, Zhang FH, Meng BB, Liu LF, Rao XS. Material removal mechanism and grinding force modelling of ultrasonic vibration

- assisted grinding for SiC ceramics. Ceram. Int. 2017, 43, 2981-2993. doi:10.1016/j.ceramint.2016.11.066.
- 83. Qiao GC, Yi SC, Zheng W, Zhou M. Material removal behavior and crack-inhibiting effect in ultrasonic vibration-assisted scratching of silicon nitride ceramics. *Ceram. Int.* **2022**, *48*, 4341–4351. doi:10.1016/j.ceramint.2021.10.229.
- 84. Xie GZ, Shang ZT, Sheng XM, Wu Y, Yu JW. Grinding Force Modeling for High-speed Deep Grinding of Engineering Ceramics. *J. Mech. Eng.* **2011**, *47*, 907–917. doi:10.3901/jme.2011.11.169.
- 85. Zhang YB, Li CH, Ji HJ, Yang XH, Yang M, Jia DZ, et al. Analysis of grinding mechanics and improved predictive force model based on material-removal and plastic-stacking mechanisms. *Int. J. Mach. Tools Manuf.* **2017**, *122*, 81–97. doi:10.1016/j.ijmachtools.2017.06.002.
- 86. Yang M, Li CH, Zhang YB, Jia DZ, Zhang XP, Hou YL, et al. Maximum undeformed equivalent chip thickness for ductile-brittle transition of zirconia ceramics under different lubrication conditions. *Int. J. Mach. Tools Manuf.* **2017**, *122*, 55–65. doi:10.1016/j.ijmachtools.2017.06.003.
- 87. Bharathi V, Anilchandra AR, Sangam SS, Shreyas S, Shankar SB. A review on the challenges in machining of ceramics. *Mater. Today Proc.* **2021**, *46*, 1451–1458. doi:10.1016/j.matpr.2021.03.019.
- 88. Xiao XZ, Zheng K, Liao WH, Meng H. Study on cutting force model in ultrasonic vibration assisted side grinding of zirconia ceramics. *Int. J. Mach. Tools Manuf.* **2016**, *104*, 58–67. doi:10.1016/j.ijmachtools.2016.01.004.
- 89. Bie WB, Zhao B, Gao GF, Chen F, Chang YL, Chen HT. Two-dimensional ultrasonic vibration-assisted dry grinding gear: Grinding force and surface characteristics. *Int. J. Adv. Manuf. Technol.* **2024**, *131*, 3021–3038. doi:10.1007/s00170-023-12882-0.
- 90. Li HT, Chen T, Li HB, Zhang YW. Influence of ultrasonic vibration on machining quality of down/up grinding in ultrasonic vibration assisted grinding of silicon carbide. *Mach. Sci. Technol.* **2023**, *27*, 1–19. doi:10.1080/10910344.2023.2194958.
- 91. Peng Y, Wu YB, Liang ZQ, Guo YB, Lin X. An experimental study of ultrasonic vibration-assisted grinding of polysilicon using two-dimensional vertical workpiece vibration. *Int. J. Adv. Manuf. Technol.* **2011**, *54*, 941–947. doi:10.1007/s00170-010-2991-x.
- 92. Tang XT, Liu YX, Shi SJ, Chen WS, Qi XD. Development of a Novel Ultrasonic Drill Using Longitudinal-Bending Hybrid Mode. *IEEE Access* **2017**, *5*, 7362–7370. doi:10.1109/access.2017.2696566.
- 93. Geng D, Lu ZH, Yao G, Liu JJ, Li Z, Zhang DY. Cutting temperature and resulting influence on machining performance in rotary ultrasonic elliptical machining of thick CFRP. *Int. J. Mach. Tools Manuf.* **2017**, *123*, 160–170. doi:10.1016/j.ijmachtools.2017.08.008.
- 94. Gao GF, Xia ZW, Yuan ZJ, Xiang DH, Zhao B. Influence of longitudinal-torsional ultrasonic-assisted vibration on micro-hole drilling Ti-6Al-4V. *Chin. J. Aeronaut.* **2021**, *34*, 254–260. doi:10.1016/j.cja.2020.06.012.
- 95. Zhao B, Bie WB, Wang XB, Chen F, Chang BQ. Design and experimental investigation on longitudinal-torsional composite horn considering the incident angle of ultrasonic wave. *Int. J. Adv. Manuf. Technol.* **2019**, *105*, 337–341. doi:10.1007/s00170-019-04220-0.
- 96. Wang JJ, Feng PF, Zhang JF, Guo P. Reducing cutting force in rotary ultrasonic drilling of ceramic matrix composites with longitudinal-torsional coupled vibration. *Manuf. Lett.* **2018**, *18*, 1–5. doi:10.1016/j.mfglet.2018.08.002.
- 97. Chen F, Bie WB, Chang YL, Zhao B, Wang XB, Zhang YM. Analytical and experimental investigation on cutting force in longitudinal-torsional coupled rotary ultrasonic machining zirconia ceramics. *Int. J. Adv. Manuf. Technol.* **2022**, *120*, 4051–4064. doi:10.1007/s00170-022-09031-4.
- 98. Bie WB, Chen F, Zhao B, Xie SX. A mechanical model of cutting force in end surface grinding of zirconia ceramics using rotary ultrasonic machining with longitudinal-torsional coupled vibration. *Int. J. Adv. Manuf. Technol.* **2023**, *127*, 651–664. doi:10.1007/s00170-023-11565-0.
- 99. Xie GZ, Huang H, Sheng XM, Mi HQ. Investigation on the Grinding Force and the Ground Damages in the High Efficiency Deep Grinding of Advanced Ceramics. *J. Hunan Univ. (Nat. Sci.)* **2008**, *35*, 26–30.
- 100. Wu SX, Zhang FL, Ni YQ, Chen F, Yan ZQ. Grinding of alumina ceramic with microtextured brazed diamond end grinding wheels. *Ceram. Int.* **2020**, *46*, 19767–19784. doi:10.1016/j.ceramint.2020.05.009.
- 101. Fu H, Jiang L, Song Q, Liu Z, Tong J, Cao C. Grinding surface roughness prediction for silicon nitride ceramics: A dynamic grinding force and frequency domain approach. *Ceram. Int.* **2023**, *49*, 35239–35253. doi:10.1016/j.ceramint.2023.08.197.
- 102. Cao JG, Wu YB, Li JY, Zhang QJ. A grinding force model for ultrasonic assisted internal grinding (UAIG) of SiC ceramics. *Int. J. Adv. Manuf. Technol.* **2015**, *81*, 875–885. doi:10.1007/s00170-015-7282-0.
- 103. Ye Z, Wen X, Wan W, Liu F, Bai W, Xu C, et al. Precision Grinding Technology of Silicon Carbide (SiC) Ceramics by Longitudinal Torsional Ultrasonic Vibrations. *Materials* **2023**, *16*, 2045–2053. doi:10.3390/ma16165572.
- 104. Sun LY, Li HS, Qiu Z, Du TH, Ma LJ. Comparative Study on Grinding Force of Two-Dimensional Ultrasonic Vibration Assisted Grinding Alumina Ceramics. *Mach. Tool Hydraul.* **2023**, *51*, 84–88.
- 105. Cheng J, Yin GQ, Wen Q, Song H, Gong YD. Study on grinding force modelling and ductile regime propelling technology in micro drill-grinding of hard-brittle materials. *J. Mater. Process. Technol.* **2015**, 223, 150–163. doi:10.1016/j.jmatprotec.2015.04.005.
- 106. Sun J, Wu YH, Zhou P, Li SH, Zhang LX, Zhang K. Simulation and experimental research on Si3N4 ceramic grinding based on different diamond grains. *Adv. Mech. Eng.* **2017**, *9*, 6789–6798. doi:10.1177/1687814017705596.
- 107. Li ZP, Zhang FH, Luo XC, Guo XG, Cai YK, Chang WL, et al. A New Grinding Force Model for Micro Grinding RB-SiC

- Ceramic with Grinding Wheel Topography as an Input. Micromachines 2018, 9, 7748-7756. doi:10.3390/mi9080368.
- 108. Wan Q, Zou L, Liu S, Wang T, Chen S, Huang Y. Investigation on abrasive wear mechanism of single diamond grain in flexible scribing titanium alloy. *Diam. Relat. Mater.* **2021**, *120*, 108631. doi:10.1016/j.diamond.2021.108631.
- 109. Zhao J, Zou L, Liu Y, Wang W, Zhang Z. Investigation of friction and wear behavior of titanium alloy-diamond based on the morphology evolution of single abrasive clusters. *Wear* **2024**, *546*–*547*, 205357. doi:10.1016/j.wear.2024.205357.
- 110. Cao Y, Zhu YJ, Ding WF, Qiu YT, Wang LF, Xu JH. Vibration coupling effects and machining behavior of ultrasonic vibration plate device for creep-feed grinding of Inconel 718 nickel-based superalloy. *Chin. J. Aeronaut.* **2022**, *35*, 332–345. doi:10.1016/j.cja.2020.12.039.
- 111. Nik MG, Movahhedy MR, Akbari J. Ultrasonic-Assisted Grinding of Ti6Al4V Alloy. *Procedia CIRP* **2012**, *1*, 353–358. doi:10.1016/j.procir.2012.04.063.
- 112. Gao T, Zhang XP, Li CH, Zhang YB, Yang M, Jia DZ, et al. Surface morphology evaluation of multi-angle 2D ultrasonic vibration integrated with nanofluid minimum quantity lubrication grinding. *J. Manuf. Process.* **2020**, *51*, 44–61. doi:10.1016/j.jmapro.2020.01.024.
- 113. Ren JX, Hua DA, Huang Q. A mathematical model of grinding force in grinding of titanium alloys. *Acta Aeronaut. Et Astronaut. Sin.* **1986**, *1*, 97–103.
- 114. Zhu LD, Yang ZC, Li ZB. Investigation of mechanics and machinability of titanium alloy thin-walled parts by CBN grinding head. *Int. J. Adv. Manuf. Technol.* **2019**, *100*, 2537–2555. doi:10.1007/s00170-018-2795-y.
- 115. Duan JH, Wu ZF, Ren JB, Zhang GC. Research on Grinding Force Prediction of Flexible Abrasive Disc Grinding Process of TC17 Titanium Alloy. *Machines* **2024**, *12*, 143. doi:10.3390/machines12020143.
- 116. Liu JL, Liu ZP, Yan YY, Wang XX. Study on the CBN Wheel Wear Mechanism of Longitudinal-Torsional Ultrasonic-Assisted Grinding Applied to TC4 Titanium Alloy. *Micromachines* **2022**, *13*, 1480. doi:10.3390/mi13091480.
- 117. Li ZH, Zhao YG, Liu GX, Cao C, Liu Q, Zhao DD, et al. Parametric Studies on Finishing of AZ31B Magnesium Alloy with Al₂O₃ Magnetic Abrasives Prepared by Combining Plasma Molten Metal Powder with Sprayed Abrasive Powder. *Micromachines* 2022, *13*, 1369. doi:10.3390/mi13091369.
- 118. Feng R. Study on grinding force in grinding titanium alloy with diamond grinding wheel. *Diam. Abras. Eng.* **2022**, *42*, 193–200.
- 119. Liu Y, Xu JY, Xiao GJ, Zhou K, Liu G. Thermo-mechanical coupling during belt grinding and corresponding surface integrity of titanium alloy. *Int. J. Adv. Manuf. Technol.* **2022**, *121*, 6599–6609. doi:10.1007/s00170-022-09783-z.
- 120. Zhang JQ, Li MH, Song PZ, Li ZH. Experimental Study on Milling-grinding Force Model of Titanium Alloy by Milling-grinding with Spherical Grinding Heads. *Tool Eng.* **2022**, *56*, 31–36.
- 121. Wang XS, Hu H, Zhang XM, Liu X. Analysis and validation of grinding force in TC4 titanium alloy surface grinding. *Manuf. Technol. Mach. Tool* **2022**, *6*, 74–79.
- 122. Huang Z, Min J, Zhou T, Yang J, Xiao LX, Li LZ. Modeling and analysis of grinding force for grinding titanium alloy with abrasive belt assisted by ultrasonic vibration. *J. Jilin Univ. (Eng. Technol. Ed.)* **2023**, *53*, 3069–3077.
- 123. Qin N, Pei ZJ, Treadwell C, Guo DM. Physics-Based Predictive Cutting Force Model in Ultrasonic-Vibration-Assisted Grinding for Titanium Drilling. *J. Manuf. Sci. Eng.* **2009**, *131*, 041011. doi:10.1115/1.3159050.
- 124. Lan T, Feng PF, Zhang JF, Zhang XY, Zheng ZP, Wang JJ. Experimental investigation on the combined effects of mechanochemical and ultrasonic vibration in titanium alloy grinding. *J. Manuf. Process.* **2024**, *121*, 382–393. doi:10.1016/j.jmapro.2024.05.049.